

# MILLIMETRIC AND SUB-MILLIMETRIC OBSERVATIONS OF IRAS 05327+3404 “HOLOEA” IN M36

O. MORATA

Institute of Astronomy and Astrophysics, Academia Sinica, P.O. Box 23-141, Taipei 106, Taiwan and  
Department of Earth Sciences, National Taiwan Normal University, 88 Sec.4, Ting Chou Rd., Taipei 116, Taiwan

Y.-J. KUAN

Department of Earth Sciences, National Taiwan Normal University, 88 Sec.4, Ting Chou Rd., Taipei 116, Taiwan

P. T. P. HO

Institute of Astronomy and Astrophysics, Academia Sinica, P.O. Box 23-141, Taipei 106, Taiwan

H.-C. HUANG

Department of Earth Sciences, National Taiwan Normal University, 88 Sec.4, Ting Chou Rd., Taipei 116, Taiwan

E. A. MAGNIER

Institute for Astronomy, University of Hawaii, 2680 Woodlawn Drive, Honolulu HI 96822

AND

R. ZHAO-GEISLER

Department of Earth Sciences, National Taiwan Normal University, 88 Sec.4, Ting Chou Rd., Taipei 116, Taiwan

*Draft version October 10, 2018*

## ABSTRACT

The transition between the proto-star, Class I, and the pre-main sequence star, Class II, phases is still one of the most uncertain, and important, stages in the knowledge of the process of formation of an individual star, because it is the stage that determines the final mass of the star. We observed the YSO “Holea”, associated with IRAS 05327+3404, which was classified as an object in transition between the Class I and Class II phases with several unusual properties, and appears to be surrounded by large amounts of circumstellar material. We used the SMA and BIMA telescopes at millimeter and sub-millimeter wavelengths to observe the dust continuum emission and the CO (1–0) and (2–1), HCO<sup>+</sup> (1–0) and (3–2), and HCN (1–0) transitions in the region around IRAS 05327+3404. We detected two continuum emission peaks at 1.1-mm: SMM 1, the sub-mm counterpart of IRAS 05327+3404, and SMM 2,  $\sim 6$  arcsec to the West. The emissions of the three molecules show marked differences. The CO emission near the systemic velocity is filtered out by the telescopes, and CO mostly traces the high-velocity gas. The HCO<sup>+</sup> and HCN emissions are more centrally concentrated around the central parts of the region, and show several intensity peaks coincident with the sub-mm continuum peaks. We identify two main molecular outflows: a bipolar outflow in an E–W direction that would be powered by SMM 1 and another one in a NE direction, which we associate with SMM 2. We propose that the SMM sources are probably Class I objects, with SMM 1 in an earlier evolutionary stage.

*Subject headings:* ISM: clouds – ISM: individual objects: IRAS 05327+3404 – ISM: jets and outflows  
– ISM: molecules – stars: protostars

## 1. INTRODUCTION

The process of the formation of an individual star has been extensively studied and modeled in the last decades, which has resulted in a well-supported general picture (see e.g., Lada & Wilking 1984; Adams et al. 1987; André et al. 1993) that describes the evolution of a young stellar object (YSO) from a pre-stellar core to a main-sequence star along several stages (Ward-Thompson 1996). These steps can be mainly divided into two main phases. First, there would be an *embedded phase*, in which a dense core in a molecular cloud collapses to form a heavily obscured, invisible to optical wavelengths, hydrostatic proto-star, surrounded by a progeni-

tor disk and a massive envelope that proceeds to accrete the majority of its mass, while simultaneously driving a highly collimated bipolar outflow. This would be followed by a *revealed phase*, after the accretion of material has stopped and once the YSO has acquired most of its final mass. The enshrouding dust is progressively cleared away and a pre-main-sequence star, surrounded by a thinning disk, becomes visible to optical and near-infrared wavelengths. In time, this proto-star will complete its Kelvin-Helmholtz contraction onto the main sequence.

A very interesting and still uncertain step in this picture is the transition between the proto-star and the pre-main-sequence star; between the embedded (Class I) and revealed (Class II) phases, which is accompanied by the

action of energetic molecular outflows and ionized jets (Magnier et al. 1999a). This stage approximately marks the end of the mass accretion onto the proto-star, which determines the final mass of the star. The mechanism that brings about this stop is not well understood yet, but it probably involves the action of the outflows on the surrounding dust and gas envelope. Thus, the observation of objects that happen to be found at this stage of the evolution is of fundamental importance to understand the physics of the processes involved and for the modeling of the disk and envelope structures around YSOs. In this paper, we present results of millimeter interferometric studies of one of these objects.

The source nicknamed “Holoëa”, Hawaiian for “flowing gas”, is a YSO associated with IRAS 05327+3404. It was discovered in optical observations of the Galactic open cluster M36 in Auriga by Magnier et al. (1996), although it is probably not associated with M36 and may be a distant member of the nearby S235 region. The distance to the object is then somewhat uncertain, ranging from the 1.2 kpc adopted by Hron (1987) for M36 to the 1.6 kpc for S235 (Blitz et al. 1982). We adopt a distance of 1.2 kpc. IRAS 05327+3404 drives a powerful ionized outflow, seen in both CO (2–1) and optical spectra, with unusually high velocity ( $\sim 650 \text{ km s}^{-1}$ ) for a low-mass star. The structure of IRAS 05327+3404 is not clear yet (see Magnier et al. 1999b). It could be a binary system, with a central star of an optical spectral type of K2 III, which is probably an FU Orionis star similar to L1551 IRS 5 (Magnier et al. 1999b), and a still embedded young star that would be powering the outflow.

The young star was classified (Magnier et al. 1999a,b) as a transitional YSO between Class I, because of the rising spectral energy distribution and a molecular bipolar outflow, and Class II YSOs, due to the visible central star and an ionized outflow. The spectral energy distribution (SED) also shows the presence of large amounts of circumstellar material, which according to optical and near-IR observations of the reflection nebula seems to be arranged in a disk with a relatively wide central hole of  $\sim 33^\circ$  opening angle. The ionized flow, the CO outflow, and the hole are all roughly aligned, and tilted by  $\sim 45^\circ$  to our line of sight (Magnier et al. 1996). Additionally, the brightness of the central star has increased  $> 1.5$  mag since the 1954 POSS plates. Magnier et al. (1999b) suggest that the source might be in the process of becoming exposed and hypothesized that the unusually wide SED can be due to the relative isolation of IRAS 05327+3404, which allowed the formation of a large circumstellar disk with high angular momentum without being disrupted by external sources. Thus, this object seems to be a good candidate to study the transition from the Class I to the Class II phase in the evolution of YSOs. Subsequent 3.6-cm VLA observations by Anglada & Rodríguez (2002) detected a source, named VLA 2, inside the error ellipsoid of IRAS 05327+3404, which coincides within  $\sim 1$  arcsec of the optical position of Magnier et al. (1996).  $\text{H}_2\text{O}$  maser emission surveys by Wouterloot et al. (1993), Codella et al. (1995) and Sunada et al. (2007) did not detect any maser emission near IRAS 05327+3404.

The structure of this paper is as follows: in Sect. 2 we describe the SMA interferometer observations made at 1-mm and the BIMA interferometer observations carried

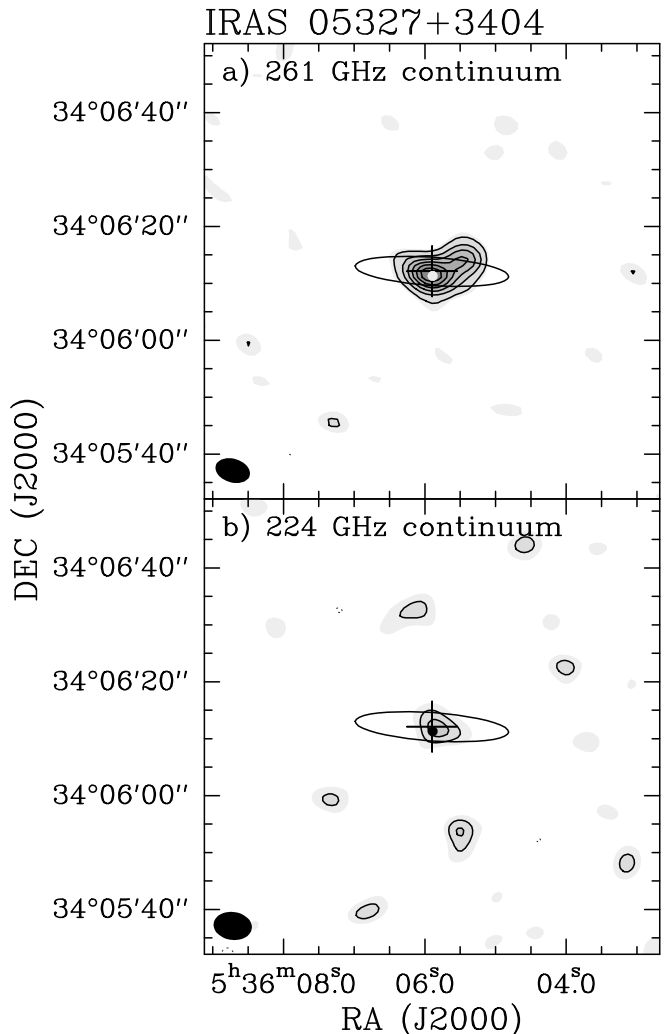


**Figure 1.** a) Map of the 1.1-mm continuum emission in the IRAS 05327+3404 region. Contours are  $-3, 3, 6, 9, \dots$  times the rms of the map,  $1.35 \text{ mJy beam}^{-1}$ . The cross marks the position of “Holoëa”, IRAS 05327+3404, and the filled (white) circle marks the position of the 3.6-cm VLA 2 source detected by Anglada & Rodríguez (2002). The central ellipse marks the error ellipse of the IRAS source. The beam size is  $\sim 6''.2 \times 4''.2$ , with a position angle,  $\text{PA} = 73.3^\circ$ . b) same as a) for the 224 GHz continuum after applying a  $w$  tapering of 36 k $\lambda$ . Contours are  $-3, 3, 4$  times the rms of the map,  $2.8 \text{ mJy beam}^{-1}$ . The beam size is  $\sim 6''.8 \times 4''.9$ , with  $\text{PA} = 82.0^\circ$ .

out in the 3-mm band; in Sect. 3 we present the results obtained of the 261 GHz continuum emission and of the CO (2–1),  $\text{C}^{18}\text{O}$  (2–1),  $\text{HCO}^+$  (2–1), CO (1–0),  $\text{HCO}^+$  (1–0), and HCN (1–0) lines; and in Sect. 4 we discuss the results and propose a picture for the structure of the gas in the region. Sect. 5 gives our conclusions.

## 2. OBSERVATIONS

### 2.1. SMA observations

The observations of IRAS 05327+3404 were performed with the eight-element SMA array (Ho et al. 2004) in Mauna Kea (Hawaii) as part of a filler-time project in November 2011 and January 2012 in the compact and sub-compact configurations, respectively. The half-power beam width of the 6-m antennas is 54 arcsec at 230 GHz, and 41 arcsec at 261 GHz. Maps were obtained with the visibility data weighted by the associated sys-

**Table 1**  
Parameters of the 2D Gaussians fitted to the 261 GHz continuum map

| Source | R.A. (J2000) | Dec. (J2000) | Gaussian <sup>a</sup><br>size | P. A. | $I_{peak}^b$<br>(Jy beam <sup>-1</sup> ) | Flux <sup>c</sup><br>(Jy) | Size <sup>d</sup><br>(arcsec) | Mass <sup>e</sup><br>( $M_{\odot}$ ) | $N(\text{H}_2)^f$<br>( $10^{23}$ cm <sup>-2</sup> ) | $n(\text{H}_2)^f$<br>( $10^6$ cm <sup>-3</sup> ) |
|--------|--------------|--------------|-------------------------------|-------|--|---------------------------|-------------------------------|--------------------------------------|---|--|
| SMM 1  | 5:36:05.93   | 34:06:11.5   | 4''0 × 2''6                   | +66°8 | 0.028                                    | 0.039                     | 3.2                           | 1.5                                  | 2.1   | 5.3  |
| SMM 2  | 5:36:05.45   | 34:06:14.2   | 2''5 × 2''3                   | -88°6 | 0.016                                    | 0.020                     | 2.4                           | 0.8                                  | 1.9   | 6.6  |

<sup>a</sup> Deconvolved major and minor axes.

<sup>b</sup> Peak intensity calculated from the fit of two 2D Gaussians to the continuum emission.

<sup>c</sup> Total integrated flux inside the 2D Gaussians resulting from the fit of the continuum emission.

<sup>d</sup> Effective diameter of the condensation from  $\sqrt{\theta_a\theta_b}$ , where  $\theta_a$  and  $\theta_b$  are the lengths of the major and minor axes of the Gaussian, respectively.

<sup>e</sup> Total mass calculated from the flux density integrated over the fitted 2D Gaussian, using the expression from Frau et al. (2010), for a distance of 1.2 kpc.

<sup>f</sup>  $N(\text{H}_2)$  and  $n(\text{H}_2)$  are the values of the column and volume densities averaged over the size of the fitted 2D Gaussian, respectively, calculated using the expressions from Frau et al. (2010), assuming dust temperature,  $T_{\text{dust}} = 15$  K, a standard dust-to-gas ratio of 100, a dust absorption coefficient at a frequency of 261 GHz,  $\kappa_{261} = 0.0089$  cm<sup>2</sup> g<sup>-1</sup>, taken as the value for dust grains with thin ice mantles for a volume density of  $\sim 5 \times 10^5$  cm<sup>-3</sup>, Ossenkopf & Henning (1994).

tem temperatures, using natural weighting. Baselines range from 6 to 53 k $\lambda$  and from 6 to 40 k $\lambda$ , respectively. The resulting synthesized beam sizes are  $\sim 2''.5$ – $6''.5$ . The total on-source observing time was of 0.99 h for the November 2011 observations and 4.62 h for the January 2012 observations. The central position of the maps for both tracks was located at  $\alpha(J2000) = 5^{\text{h}}36^{\text{m}}05^{\text{s}}.90$ ,  $\delta(J2000) = +34^{\circ}06'12''.1$ .

The receivers were tuned to a rest frequency of 230.53797 GHz for the observations in November 2011 and to 267.55762 GHz for the observations in January 2012, Doppler tracked to a velocity  $V_{\text{LSR}}$  of  $-21.7$  km s<sup>-1</sup>. In the 230.5 GHz observations, the correlator was configured to observe three spectral windows to include the CO (2–1), <sup>13</sup>CO (2–1), and C<sup>18</sup>O (2–1) lines, with 203 kHz (0.26 km s<sup>-1</sup>) resolution; 3.94 GHz were dedicated to observe the 1.3 mm continuum in both the upper and lower sidebands. For the 267.5 GHz observations, the correlator was configured to observe 4 spectral windows: three windows with 203 kHz (0.23 km s<sup>-1</sup>) spectral resolution, including the HCO<sup>+</sup> (3–2) line, and one window with 812 kHz (0.91 km s<sup>-1</sup>). 3.94 GHz were dedicated to observe the 1.1 mm continuum, in both the upper and lower sidebands.

The data were reduced using the MIR and MIRIAD (Sault et al. 1995) packages. The data were flagged for bad channels, antennas, weather, and pointing. We used 3C84 and BL Lac as bandpass calibrators for the November 2011 track and 3C279, Mars, and 0927+390 for the January 2012 track. Gain calibrators were 0646+448 and 0530+135 for the November 2011 data and 3C111 for January 2012. Absolute flux calibration was done using observations of Uranus in both tracks.

## 2.2. BIMA observations

The observations of IRAS 05327+3404 were carried out with the BIMA array at the Hat Creek Radio observatory during 6 periods, using 6 antennas in the C configuration in August 1995 (twice) and September 1995, and using 9 antennas in the H configuration in December 1995 and May 1996 (twice). Maps were done at 88 and 115 GHz with the visibility data weighted by the associated system temperatures, using natural weighting, and applying the primary beam correction. The  $uv$ -coverage was  $\sim 1.2$ – $37$

k $\lambda$ , and the resulting synthesized beam sizes are  $\sim 6$ – $10$  arcsec. The half-power beam width of the BIMA antennas is 120 arcsec at 100 GHz. The central position of the maps was also located at  $\alpha(J2000) = 5^{\text{h}}36^{\text{m}}05^{\text{s}}.90$ ;  $\delta(J2000) = +34^{\circ}06'12''.1$ .

Two frequency setups were used, centered at 88 and 115 GHz, respectively. The target molecular lines were CO (1–0) at 115.27120 GHz, HCO<sup>+</sup> (1–0) at 88.18852 GHz, and HCN (1–0) at 88.63185 GHz. The digital correlator was configured to observe simultaneously several molecular line transitions in the upper side band (USB) at spectral resolutions of 97.7 and 390.6 kHz/channel, which correspond to velocity resolutions of 0.25 and 1.00 km s<sup>-1</sup> for CO, and 0.32 and 1.28 km s<sup>-1</sup> for HCO<sup>+</sup> and HCN. CO lines were observed in one period in August 1995 and in September 1995.

Calibration and data reduction were performed using the MIRIAD software package. The source 0530+135 was used as phase calibrator, while Mars, Saturn, 3C273, and 0530+135 were used as band-pass calibrators. The molecular line transitions tuned to the lower side band (LSB) did not show any emission.

## 3. RESULTS

### 3.1. Continuum observations

#### 3.1.1. 261 and 224 GHz continuum

Figure 1a shows the continuum map of IRAS 05327+3404 obtained with the SMA from the combination of the continuum data from the USB and LSB at a nominal frequency of 261 GHz. The only emission over  $3\sigma$  is located in the central 10 arcsec of the map. The emission is extended in an East–West direction with a slightly NW bend in the Western tip. The emission peak (SMM 1) is located at  $\sim 1''.1$  S of the catalog position of IRAS 05327+3404 with an intensity of 28.7 mJy beam<sup>-1</sup> ( $\sim 21\sigma$ ). There is a secondary emission peak (SMM 2) located at an offset,  $\Delta\alpha, \Delta\delta = (-5''.2, +3''.1)$  from SMM 1, with an intensity of 17.4 mJy beam<sup>-1</sup> ( $\sim 13\sigma$ ). The separation between the two peaks is  $\sim 6''.1$ , about  $\sim 7300$  AU at the assumed distance to the source, and it probably indicates the presence of two objects. The total flux inside the half-intensity contour encompassing both emission peaks is 33.4 mJy.

We tried to see if the continuum emission could be des-

cribed by the superposition of two elliptical Gaussians centered around the position of the two emission peaks. Table 1 shows the parameters of the two 2-D Gaussians that best reproduce the continuum emission over  $3\sigma$ : the one corresponding to SMM 1 is elongated in a NE-SW direction, while the one corresponding to SMM 2 is almost circular in shape. The central positions, which we adopt as the nominal positions of the sub-mm sources, are slightly displaced with respect to the visual identification we had made, but well inside our angular resolution. The total integrated fluxes we measure are 39.1 and 19.9 mJy, respectively.

The catalog position of IRAS 05327+3404 is located  $\sim 0.8$  arcsec NW from SMM 1, while the unresolved 3.6-cm VLA 2 source detected by Anglada & Rodríguez (2002) is located  $\sim 0.5$  arcsec SW of SMM 1. The uncertainty in the determination of the VLA position is probably of the order of  $\sim 1$  arcsec, given the beam size and signal-to-noise ratio of the cm observations. We would also expect that if the unresolved VLA 2 source had any significant contribution from SMM 2, the centroid of the centimeter emission would be displaced  $> 1$  arcsec to the NW. Thus, given that the positions of the infrared and centimeter emissions coincide within  $\sim 1$  arcsec from SMM 1, we conclude that SMM 1 is the sub-mm counterpart of IRAS 05327+3404 and VLA 2.

Figure 1b shows the continuum map obtained by combining the USB and LSB continuum data in the 230.5 GHz track, with a resulting nominal frequency of 224 GHz, after applying a  $uv$  tapering of 36 k $\lambda$ . We do not find any extended emission on the map obtained with natural weighting. After applying the tapering, we find a condensation  $\sim 7.5 \times 5.5$  arcsec, coinciding with the position of SMM 1, with an intensity peak of 12.7 mJy beam $^{-1}$  and an estimated total flux of 18.9 mJy (measured at the  $2\sigma$  contour).

### 3.1.2. 3-mm continuum

The lines tuned up in the lower side band of both of the frequency setups used with the BIMA telescope, at 85 and 112 GHz, respectively, were too weak to be detected. The 768 channels available in four windows in the LSB could then be used to try to detect continuum emission. Unfortunately, the bandwidth was probably too narrow to detect any emission over  $3\sigma$  ( $1\sigma$  is 3.8 and 20 mJy beam $^{-1}$  respectively) in the region. Adding the visibilities at the two frequencies in order to get a better signal-to-noise ratio using a multi-frequency cleaning did not improve the results and we failed to detect any emission over  $3\sigma$  ( $1\sigma = 4.9$  mJy beam $^{-1}$ ).

## 3.2. Spectral observations

### 3.2.1. $\text{HCO}^+$ (3-2)

Figure 2 shows the integrated intensity map of the  $\text{HCO}^+$  (3-2) emission obtained with the SMA. The emission is elongated in the NW-SE direction, with two partially resolved condensations. The more intense (peak intensity 3.38 Jy beam $^{-1}$ ) coincides with the position of the 1.1-mm continuum emission peak SMM 1. The second condensation (peak intensity 1.43 Jy beam $^{-1}$ ) is located  $\sim 8.5$  arcsec NW of the emission peak. Both condensations are connected by low level emission at more than the  $3\sigma$  level of the map. The continuum emission

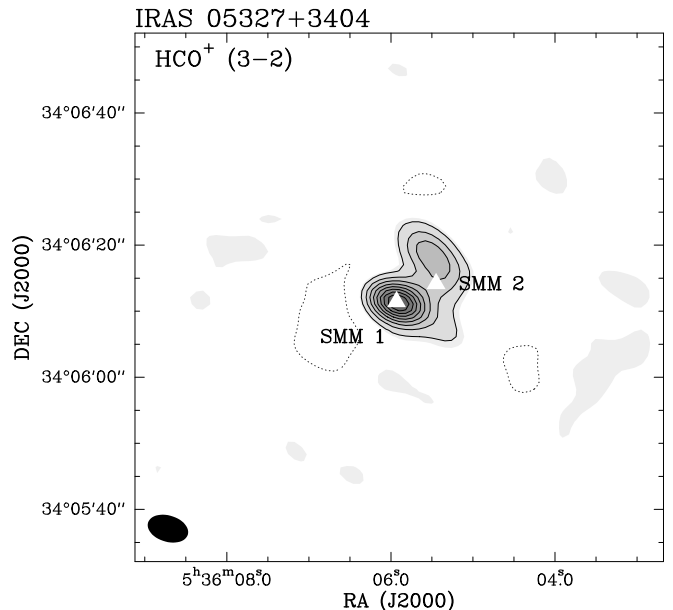


**Figure 2.** Integrated intensity map of the  $\text{HCO}^+$  (3-2) emission in the velocity range from  $-23.99$  to  $-19.21$  km s $^{-1}$ , with a resulting mean velocity of  $-21.6$  km s $^{-1}$ . Contours are  $-3, 3, 6, 9, \dots$  times the rms of the map,  $0.12$  Jy beam $^{-1}$ . The beam size is  $\sim 6''.3 \times 4''.0$ , with PA =  $73.3^\circ$ . The triangles mark the positions of the emission peaks in the 261 GHz continuum map, SMM 1 and SMM 2 (Fig. 1a).

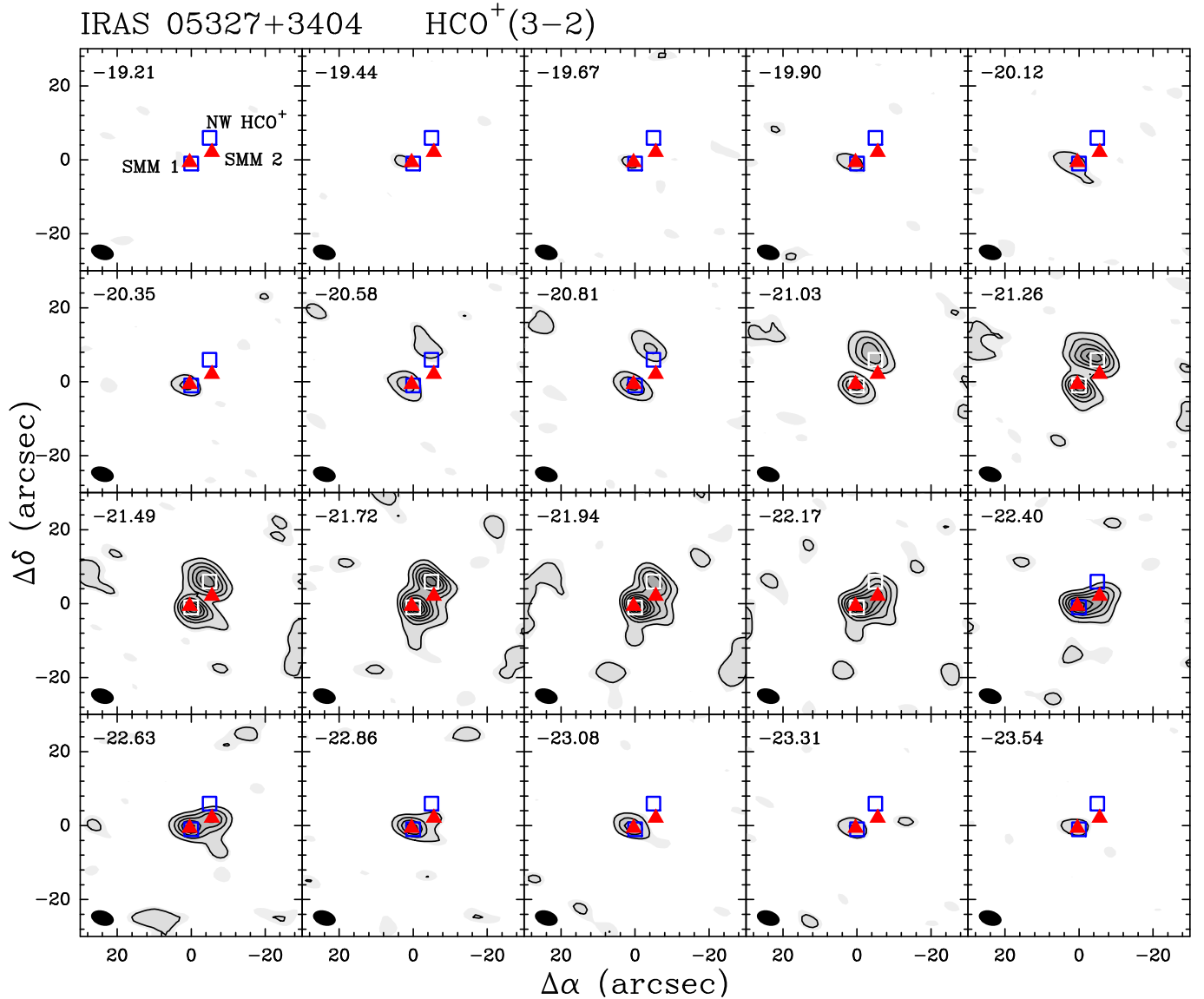
peak SMM 2 is located approximately at the neck of this bridge.

Figure 3 shows the channel maps of the  $\text{HCO}^+$  (3-2) emission from  $-23.8$  to  $-19.2$  km s $^{-1}$ . The two condensations found in the integrated intensity map (Fig. 2) are present in the central velocity channels. The central condensation is seen in all the channels containing any emission, while there is emission over a  $3\sigma$  level  $\sim 7.5$  arcsec to the NW only from  $-22.17$  to  $-20.58$  km s $^{-1}$ . This emission coincides with the secondary condensation found in the integrated intensity map and seems to drift slightly from the SW to the NE. There is a third condensation only found in the more blue-shifted emission (from  $-22.63$  to  $-22.17$  km s $^{-1}$ ) just south of the peak of the secondary condensation, located  $\sim 5.5$  arcsec to the NW of SMM 1, and coinciding with the position of SMM 2 (see Fig. 1). All three condensations are connected by emission at levels  $> 6\sigma$  for velocities closer to the systemic velocity. We also find some weak extended emission elongated in a N-S direction just South of SMM 1 at the systemic velocity channel ( $-21.72$  km s $^{-1}$ ) and some towards the SW from a position in-between SMM 1 and SMM 2 at  $-22.53$  km s $^{-1}$ .

### 3.2.2. $\text{HCO}^+$ (1-0)

Figure 4 shows the integrated intensity map of the emission of the  $\text{HCO}^+$  (1-0) transition obtained with BIMA. The more intense emission is oriented in the NW-SE direction, enclosing the emission peaks found in the  $\text{HCO}^+$  (3-2) maps. There are two emission peaks, the most intense one is located to the NW of SMM 1, at  $(\Delta\alpha, \Delta\beta) = (-6''.4, +4''.2)$ , and it seems to include the two northwestern peaks found in the  $\text{HCO}^+$  (3-2) maps. The second emission peak coincides within uncertainties with SMM 1.





**Figure 3.** Channel maps of the  $\text{HCO}^+$  (3–2) emission in the velocity range from  $-23.54$  to  $-19.21$   $\text{km s}^{-1}$ . Contours are  $-3, 3, 6, 9, \dots$  times the rms of the map,  $0.26 \text{ Jy beam}^{-1}$ . The beam size is  $\sim 6''.3 \times 4''.0$ , with  $\text{PA} = 73.3^\circ$ . The triangles mark the positions of the emission peaks in the 261 GHz continuum map (Fig. 1a) and the squares mark the positions of the emission peaks of the integrated intensity map of  $\text{HCO}^+$  (3–2). The velocity, in  $\text{km s}^{-1}$ , of each map is indicated in the upper left corner of each panel.

The channel maps of the  $\text{HCO}^+$  (1–0) line (see Fig. 5) also show the three condensations found in the (3–2) line, surrounded by more extended emission, which always connects the three main peaks. The central condensation is mainly found from  $-22.42$  to  $-21.43$   $\text{km s}^{-1}$ , and in particular around the systemic velocity. The emission towards the NW is predominantly found in the red-shifted velocities, from  $-21.76$  to  $-20.78$   $\text{km s}^{-1}$ . The emission around SMM 2 is particularly intense for the blue-shifted velocities, from  $-22.42$  to  $-21.76$   $\text{km s}^{-1}$ . There are other emission features in the blue-shifted channels, which were also seen in the  $\text{HCO}^+$  (3–2) channel maps: an elongation in a N–S direction south of SMM 1, with a local emission peak; and an elongation to the SW from a point in-between SMM 1 and SMM 2. There is also a weak emission patch elongated to the NE of SMM 1 at  $-22.42$   $\text{km s}^{-1}$ .

There is also fainter emission at  $\sim 50$  arcsec NW of

SMM 1, approximately coincident with emission also found in  $\text{HCN}$  (1–0) and  $\text{CO}$  (1–0) (see Sects. 3.2.3 and 3.2.4, respectively). This emission patch only appears in the velocity range  $-22.09$  to  $-21.11$   $\text{km s}^{-1}$ , but the emission peak moves  $\sim 10$  arcsec from W to E as the velocity changes from red- to blue-shifted channels.

### 3.2.3. $\text{HCN}$ (1–0)

The emission of the  $\text{HCN}$  (1–0) line obtained with the BIMA telescope (Fig. 6) is very concentrated in the central part of the map, in the shape of an “L” that connects the two continuum peaks and the NW  $\text{HCO}^+$  (3–2) emission peak. None of these three emission peaks coincides with the  $\text{HCN}$  emission peak, which is located  $\sim 4''$  to the NW of SMM 1, midway between SMM 1 and SMM 2. The NW  $\text{HCO}^+$  (3–2) peak is seen as an emission plateau to the N. There is also faint emission at  $\sim 50$  arcsec NW of IRAS 05327+3404, coinciding with the  $\text{HCO}^+$  (1–0)

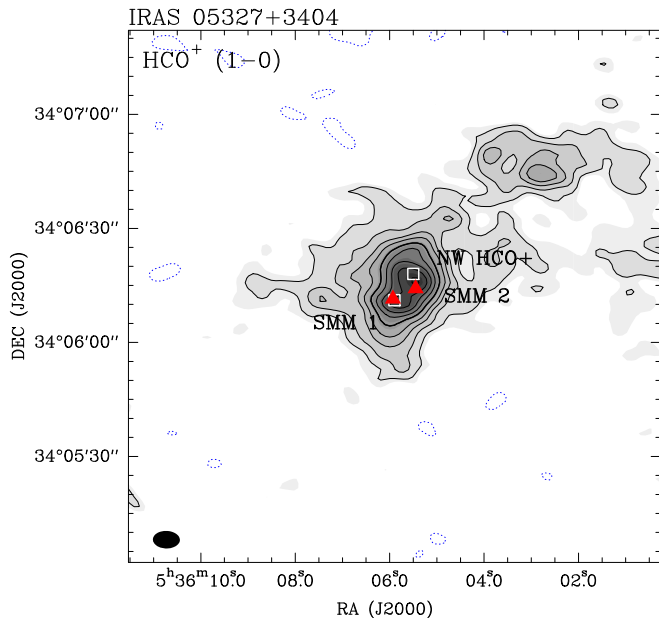


**Figure 4.** Map of the integrated intensity of the  $\text{HCO}^+(1-0)$  emission in the velocity range from  $-22.42$  to  $-20.78$   $\text{km s}^{-1}$ , with a resulting mean velocity of  $-21.60$   $\text{km s}^{-1}$ . The contours are  $-3, 3, 4, \dots, 7, 9, \dots, 15, 19, 21, 22, 23, 24$  times the rms of the map,  $0.060$   $\text{Jy beam}^{-1}$ . The triangles mark the position of the continuum peaks and the squares mark the position of the  $\text{HCO}^+(3-2)$  emission peaks. The beam size is  $\sim 7''.1 \times 4''.6$ , with  $\text{PA} = 88.6^\circ$ .

emission patch.

Figure 7 shows the channel maps of the emission of the  $\text{HCN}(1-0)$  line in the range from  $-22.48$  to  $-20.82$   $\text{km s}^{-1}$ . The emission tends to be very concentrated and shows some similarities to the  $\text{HCO}^+$  channel maps. The  $\text{HCN}(1-0)$  emission close to SMM 2 is predominantly red-shifted to the N, closer to the position of the NW  $\text{HCO}^+(3-2)$  peak, and predominantly blue-shifted to the S of the source. Only the central channel maps show any, and weaker, emission around the position of SMM 1. The central velocity channel map also shows a weak condensation or local emission peak  $\sim 10$  arcsec South of SMM 1, approximately at the position of a similar condensation found in the channel maps of  $\text{HCO}^+$ .

### 3.2.4. $\text{CO}(1-0)$

The map of the  $\text{CO}(1-0)$  emission obtained with BIMA (Fig. 8) shows a very different distribution from the maps of  $\text{HCO}^+$  and  $\text{HCN}$ . The  $\text{CO}$  emission is mainly found in an East-West strip passing towards the West through the position of SMM 1, and then bending in a SW direction West of SMM 1. The main emission peak is located  $\sim 3$  arcsec NE of SMM 1. There is a small spur in the emission in the NW direction from the position of IRAS 05327+3404, which roughly corresponds to the more intense emission found in the  $\text{HCO}^+(1-0)$  and  $\text{HCN}(1-0)$  integrated intensity maps. A weaker emission peak is found  $\sim 18$  arcsec East of SMM 1. There is also a weak emission peak at  $\sim 15$  arcsec SW of SMM 1, in a similar direction as some weakly extended emission found in the  $\text{HCO}^+$  channel maps. There are several clumps of emission in the NE direction from IRAS 05327+3404, with a position angle ( $\text{PA}$ )  $\sim 9^\circ$ . Another patch of emission is located  $\sim 50$  arcsec NW of IRAS 05327+3404,

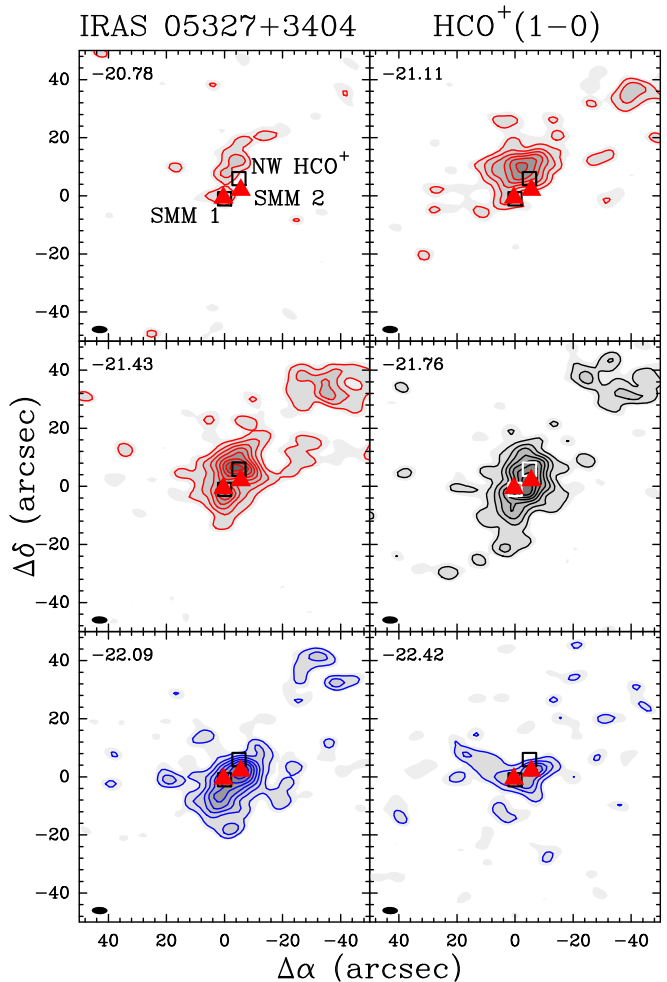


**Figure 5.** Channel maps of the  $\text{HCO}^+(1-0)$  line in the velocity interval  $-22.42$  to  $-20.78$   $\text{km s}^{-1}$ . The first contour is  $0.447$   $\text{Jy beam}^{-1}$  with contour increments of  $0.298$   $\text{Jy beam}^{-1}$ . The triangles mark the position of the continuum peaks and the squares mark the position of the  $\text{HCO}^+(3-2)$  emission peaks. The peak intensity is found at  $v_{\text{LSR}} = -21.43$   $\text{km s}^{-1}$ , at  $(\Delta\alpha, \Delta\beta) = (-3''.5, +6'')$ , with an intensity of  $2.7$   $\text{Jy beam}^{-1}$ . The velocity, in  $\text{km s}^{-1}$ , of each map is indicated in the upper left corner of each panel.

coinciding with similar emission patches found in the  $\text{HCO}^+(1-0)$  and  $\text{HCN}(1-0)$  maps.

If we compare with the JCMT  $\text{CO}(2-1)$  integrated intensity map of Magnier et al. (1999b), our observations cover the more central regions closer to IRAS 05327+3404. Taking into account the lower angular resolution of the single-dish map, the distribution of the BIMA emission seems to be similar, but it is also clear that we are probably missing some extended emission. The  $\text{CO}(1-0)$  emission that we find along the NE direction follows the same direction as the NE outflow that was identified by Magnier et al. (1999b). We are tracing the innermost part of this outflow and the clumps we identify coincide with local intense emission in the map of Magnier et al. (1999b).

Figure 9 shows the 4-channel ( $0.25$   $\text{km s}^{-1}$ /channel) averaged intensity maps of  $\text{CO}$  centered on the position of IRAS 05327+3404. The channel at the systemic velocity,  $v_{\text{LSR}} = -21.77$   $\text{km s}^{-1}$ , does not have any emission of  $\text{CO}$  in the central positions. This is probably due to an

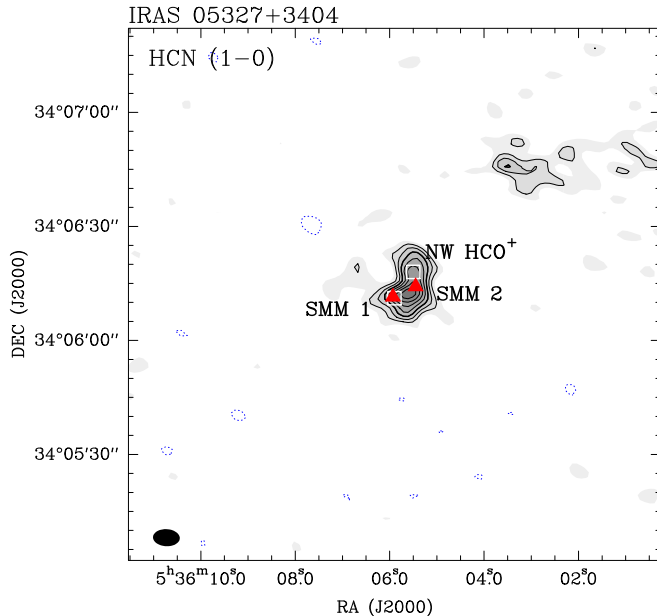


**Figure 6.** Map of the integrated intensity of the HCN (1–0) emission in the velocity range from  $-22.15$  to  $-21.15$   $\text{km s}^{-1}$ , with a resulting mean velocity of  $-21.65$   $\text{km s}^{-1}$ . The contours are  $-3, 3, 4, \dots, 9$  times the rms of the map,  $0.065$   $\text{Jy beam}^{-1}$ . The triangles mark the position of the continuum peaks and the squares mark the position of the  $\text{HCO}^+$  (3–2) emission peaks. The beam size is  $\sim 7''.1 \times 4''.5$ , with a  $\text{PA} = 87^\circ$ .

extended gas structure at this position at about the systemic velocity, which is filtered by the BIMA telescope (see Sect. 4.4.1). On the other hand, the red- and blue-shifted emission channel maps reveal a very complex velocity structure. In order to examine more carefully the velocity structure of the region, we show in Fig. 10a the superposition of the integrated intensity of the red- and blue-shifted channels with significant emission of CO and motions larger than  $1$   $\text{km s}^{-1}$  relative to the systemic velocity. We further show in Figs. 10b and 10c the red- and blue-shifted integrated intensity maps for the high- and low-relative velocities with respect to the systemic velocity, respectively.

Two outflows can be identified in the data: a bipolar outflow elongated in the East-West direction on both sides of SMM 1, accounting for most of the high-velocity emission in Fig. 10, and another one in the NE direction, at an angle of  $\sim 9^\circ$ , from which we seem to detect only the red-shifted lobe. These two outflows had also been detected in CO (2–1) by Magnier et al. (1999b), but at much lower angular resolution. We also find that the relative high-velocity emission is in general more compact than the relative low-velocity emission (see Figs. 10b and 10c).

The red-shifted “arm” of the East-West outflow extends eastwards up to  $\sim 45$  arcsec at low relative velocities,  $\sim 20$  arcsec for the high-relative velocities (see Figs. 9 and 10). The blue-shifted “arm” is more clearly seen at low-relative velocities (Fig. 10c) and it extends to  $\sim 25$  arcsec westwards. Figure 10c shows the overlap between the red- and blue-shifted lobes over the position of SMM 1.

The NE outflow is more clearly seen at low-relative velocities (see Figs. 9 and 10c). The maps at  $-19.74$   $\text{km s}^{-1}$  in Fig. 9 and Fig. 10c also show that the outflow is not

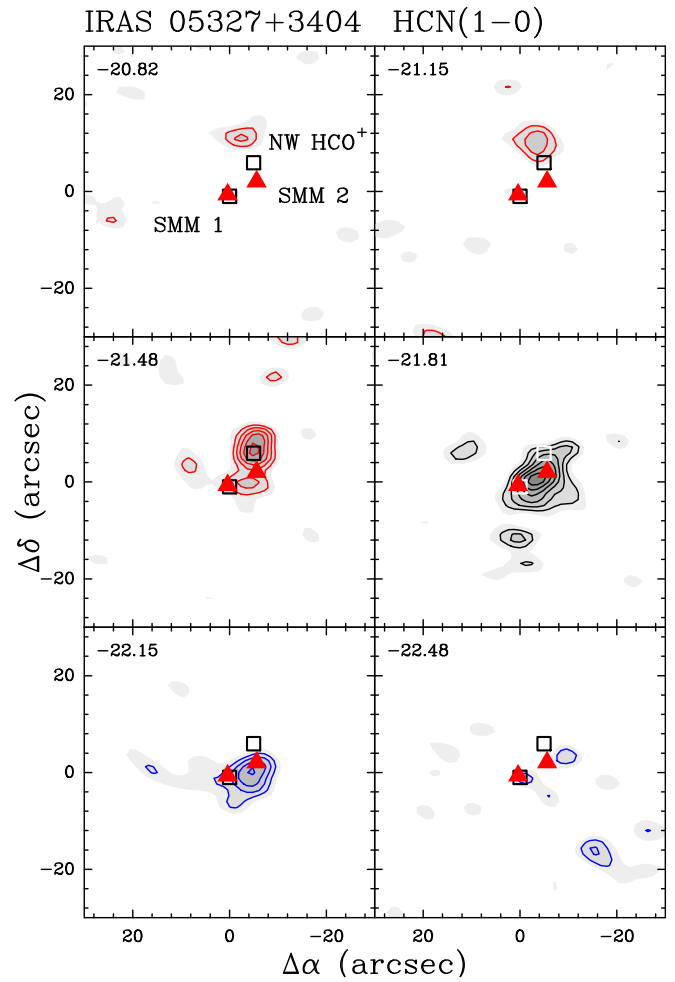


**Figure 7.** Channel map of the HCN (1–0) line in the velocity interval from  $-22.48$  to  $-20.82$   $\text{km s}^{-1}$ . The contours are  $-3, 3, 4, \dots, 7$  times the rms of the maps,  $0.129$   $\text{Jy beam}^{-1}$ . The triangles mark the position of the continuum peaks and the squares mark the position of the  $\text{HCO}^+$  (3–2) emission peaks. The peak emission is found at  $-21.81$   $\text{km s}^{-1}$ , at  $(\Delta\alpha, \Delta\delta) = (-3'', 0'')$ , with a flux density of  $1.11$   $\text{Jy beam}^{-1}$ . The velocity, in  $\text{km s}^{-1}$ , of each map is indicated in the upper left corner of each panel.

aligned with the position of SMM 1, but it is better aligned with the position of SMM 2, a few arcsec to the West of SMM 1.

There are other velocity structures in our data that could be tracing more outflows, but they are not so clearly defined. Fig. 10b shows red-shifted emission extending  $\sim 10$  arcsec to the SE of SMM 1, which is also found in the low-relative velocity emission map (Fig. 10c). The high-relative velocity emission map also shows compact,  $\sim 10$  arcsec, blue-shifted emission elongated in a N–S direction originating from around SMM 1 (see Fig. 10b). These red- and blue-shifted components could be roughly aligned, but it is very difficult to tell if they belong to independent outflows or are part of emission related to the two other outflows. Finally, the channel map at  $-20.75$   $\text{km s}^{-1}$  shows a spur pointing away towards the SW from the central position of the map. The higher intensity contours point towards the position of SMM 2 and the NW  $\text{HCO}^+$  peak, but the lower emission contours are connected to the position of SMM 1.

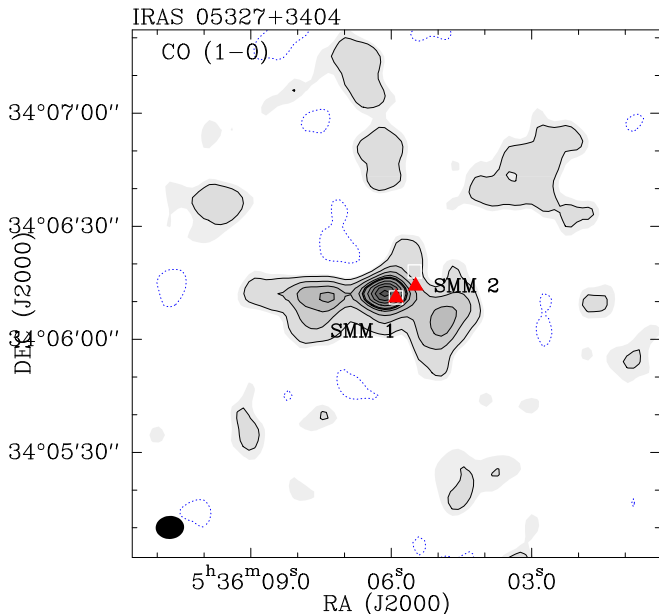


**Figure 8.** Integrated intensity of the CO (1–0) emission in the velocity range from  $-27.47$  to  $-15.04$   $\text{km s}^{-1}$ , with a resulting mean velocity of  $-21.01$   $\text{km s}^{-1}$ . The contours are  $-3, 3, 6, 9, \dots$  times the rms of the map,  $0.075$   $\text{Jy beam}^{-1}$ . The triangles mark the position of the continuum peaks and the squares mark the position of the  $\text{HCO}^+$  (3–2) emission peaks. The beam-size is  $\sim 7''.6 \times 6''.2$ , with a PA =  $-86.4^\circ$ . The peak emission is located at a position  $(\Delta\alpha, \Delta\beta) = (+2'', 0'')$  with an intensity of  $2.14$   $\text{Jy beam}^{-1}$ .

Additionally, we find several patches of blue-shifted emission strewn around the central position, mostly in the NE and NW quarters at  $-22.79$  and  $-23.80$   $\text{km s}^{-1}$ . These emission patches probably trace more extended material partially filtered out by the telescope.

### 3.2.5. CO (2–1)

Figure 11 shows the CO (2–1) integrated intensity map obtained with the SMA in the velocity interval  $-25.0$  to  $-13.8$   $\text{km s}^{-1}$ . The only significant emission is found in an E–W direction very close to SMM 1. The emission peak is located  $\sim 2.5$  arcsec West of SMM 1. There are not any other clearly detected structures in the map, possibly due to the limited observing time obtained with the SMA.

Figure 12 shows the 4-channel averaged intensity maps of the CO (2–1) line. The emission is mainly found around the central position of the map, along the East–West direction through the position of IRAS 05327+3404, in a way very similar to the one found in the CO (1–0) line: most of the emission is found in the red-shifted velocities in a East–West strip located to the West of IRAS 05327+3404 and originating from the position of SMM 1. The channels near the systemic velocity,  $-21.76$   $\text{km s}^{-1}$ , do not have any emission. There is also some weaker emission in the blue-shifted maps more or less symmetrical to the emission found in the red-shifted maps. The red- and blue-shifted emissions overlap on the position of SMM 1, which supports the identification of SMM 1 as the powering source of the E–W outflow.

### 3.3. Spectra

Figure 13 shows the spectra of the five molecular lines we detected ( $\text{HCO}^+$  1–0,  $\text{HCO}^+$  2–1, HCN 1–0, CO 1–0, and CO 2–1) obtained at four selected positions of our

maps: the sub-millimeter peaks, SMM 1 and SMM 2, the NW  $\text{HCO}^+$  peak, and the CO peak. We can appreciate the absorption dip in the CO emissions at the systemic velocities, where the  $\text{HCO}^+$  and HCN emissions are found. We can also see the broadening of the  $\text{HCO}^+$  (3–2) line at the SMM 1 position and, especially, at the position of the CO peak (see Sect. 4.3). Line-widths for HCN are  $\sim 0.7 - 1.1$   $\text{km s}^{-1}$ , while the line-widths for  $\text{HCO}^+$  are  $\sim 1.0 - 1.1$   $\text{km s}^{-1}$  at the SMM 2 and NW  $\text{HCO}^+$  positions, and  $\sim 1.4 - 2.0$   $\text{km s}^{-1}$  at the positions of SMM 1 and the CO peak (see Sect. 4.3).

## 4. DISCUSSION

### 4.1. Dust continuum emission

We calculated the mass of the molecular gas from the 1.1-mm continuum emission, using the flux density and emission sizes measured from fitting two 2D-Gaussians to the continuum map. Table 1 gives the  $\text{H}_2$  mass, and  $\text{H}_2$  averaged column and volume densities for the two condensations found in the 261 GHz continuum map. Given the presence of stellar objects embedded in the dust emission, we assumed a dust temperature of 15 K and a dust absorption coefficient for dust with thin ice mantles at 261 GHz,  $\kappa_{261} = 0.0089$   $\text{cm}^2 \text{g}^{-1}$  (Ossenkopf & Henning 1994). We estimate a mass of  $1.5 M_\odot$  for SMM 1 and  $0.8 M_\odot$  for SMM 2. The uncertainties in the determination of the dust temperature represent an uncertainty in the mass calculation of about a factor of 2. For dust temperatures of 10–20 K, the estimated masses would be between  $2.9 - 1.0 M_\odot$  and  $1.5 - 0.5 M_\odot$ , respectively. These estimates assume a very simple spherical structure for the envelope of these sources. The real distribution of the gas around the SMM sources probably includes the presence of circumstellar disks, and the mass in the proto-stellar objects, which would add some uncertainties to the mass determination.

Magnier et al. (1996) gave a range of values for the bolometric luminosity of IRAS 05327+3404,  $L_{\text{bol}} \sim 41 - 82 L_\odot$ . As we have shown in Fig. 1, the IRAS error ellipse includes both SMM 1 and SMM 2, and it is conceivable that this bolometric luminosity has contribution from both sources. In the following discussion, we assume that most of the  $L_{\text{bol}}$  is associated with SMM 1, while  $L_{\text{bol}}$  for SMM 2 is not easy to define.

In order to see if we could shed more light on the evolutionary stages of the SMM sources, we have compared the values of the mass from the sub-mm dust continuum with the envelope mass vs. bolometric luminosity plot shown in Fig. 1 of Bontemps et al. (1996). We define as envelope mass,  $M_{\text{env}}$ , the mass derived from our sub-mm dust emission observations. Interestingly, SMM 1 would be located in the region mainly occupied by the Class 0 sources, while SMM 2 would be at the border between the regions where Class 0 and Class I are found. The uncertainty in the determination of the envelope mass is more important to classify SMM 2 than the uncertainty in the determination of its bolometric luminosity (which we expect to be lower than that of SMM 1): a lower value for the calculated envelope mass will set SMM 2 deeper into the Class I region.

### 4.2. The molecular outflows: CO emission

The results of the CO (1–0) data shown in Sect. 3.2.4 strongly indicate that there are several outflows in the re-



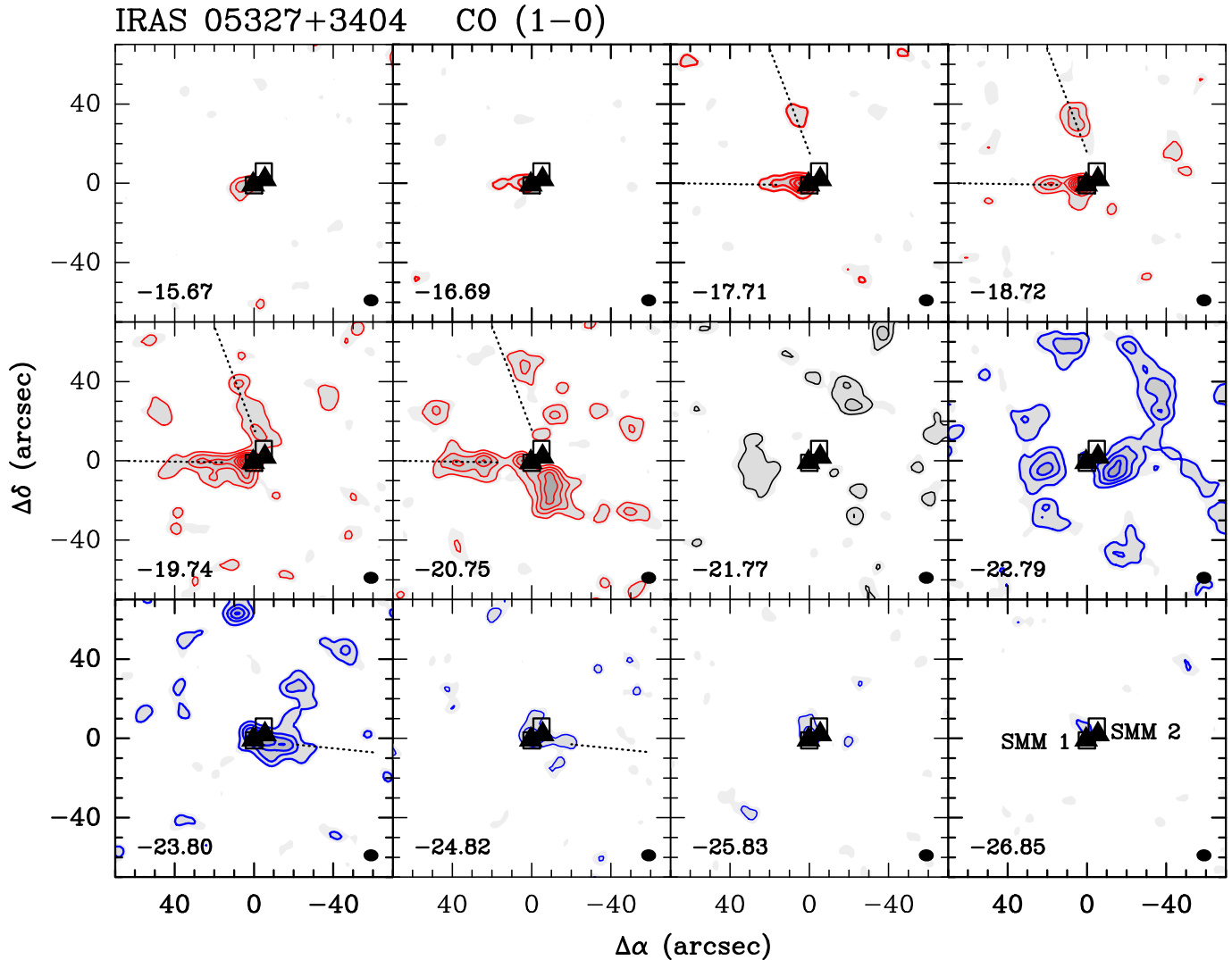


**Figure 9.** Maps of the 4-channel ( $0.25 \text{ km s}^{-1}/\text{channel}$ ) average of the CO (1–0) lines in the velocity interval from  $-26.85$  to  $-15.67 \text{ km s}^{-1}$ . The contours are 3, 6, 9, ... times the rms of the map,  $0.24 \text{ Jy beam}^{-1}$ . The triangles mark the position of the continuum peaks and the squares mark the position of the  $\text{HCO}^+$  (3–2) emission peaks. The peak emission is located at  $v_{\text{LSR}} = -19.74 \text{ km s}^{-1}$  at  $(\Delta\alpha, \Delta\beta) = (+2'', 0'')$ , with a flux density of  $5.04 \text{ Jy beam}^{-1}$ . The dotted straight lines mark the directions of possible outflow arms. The velocity, in  $\text{km s}^{-1}$ , of each map is indicated in the upper left corner of each panel.

gion around IRAS 05327+3404, with probably different inclinations with respect to the plane of the sky, and, correspondingly, there should be several objects powering them. To summarize, we have clearly identified two molecular outflows: one in an East-West direction, around SMM 1, which seems to be the more promising candidate to power this outflow; and another outflow elongated in a NE direction, with a  $\text{PA} = 9^\circ$ , aligned with SMM 2, which is also the best candidate to power the outflow. Additionally, there are indications of other kinematic structures, but our data are not complete enough to clearly identify the nature of these structures: the “SW arm” found in the CO (1–0) data; the compact blue-shifted emission in a N–S direction North of SMM 1; and the compact red-shifted emission SE of SMM 1.

Figure 14 shows the P-V cuts we took along the red- and blue-shifted elongated structures. The missing CO emission in the central regions of the map is very apparent in the velocity range  $\sim -22.9$  to  $\sim -21.4 \text{ km s}^{-1}$ , which makes it very difficult to analyze what is really

happening near IRAS 05327+3404. Fig. 14a shows the P-V cut in the direction of the optical outflow,  $\text{PA} = 9^\circ$ . Similarly to what Magnier et al. (1999b) found in their data, the outflow velocity increases in relative velocity with the distance from the central region. But, we also find that at larger distances the velocity decreases with distance. On the opposite side of the central region, there is a small gradient in the red-shifted velocities that probably points to the SW “outflow” found in the CO emission channel maps (see Fig. 9). The CO lines are very broad at the central position with velocities from  $\sim -26.5$  to  $\sim -23 \text{ km s}^{-1}$  and from  $\sim -20.5$  to  $\sim -16 \text{ km s}^{-1}$ , which indicates that the CO emission is probably tracing the outflowing gas there.

Figure 14b shows the P-V cut obtained through the central position following an approximate East–West direction. From this P-V cut, the peak emission could be displaced  $\sim 2\text{--}3 \text{ arcsec}$  to the East. This position would coincide with the region where  $\text{HCO}^+$  shows line broadening, East of SMM 1 (see Sect. 4.3). This P-V

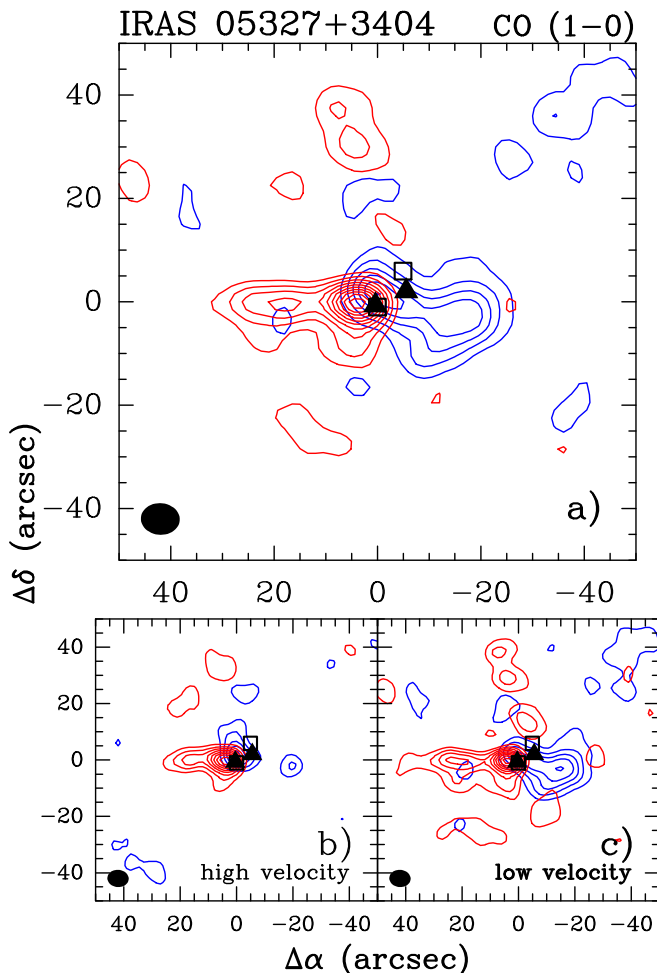


**Figure 10.** *a)* Map overlapping the integrated emission of the red- (from  $-20.63$  to  $-15.80$   $\text{km s}^{-1}$ ) and blue-shifted (from  $-26.22$  to  $-22.66$   $\text{km s}^{-1}$ ) channels of the CO (1–0) line in IRAS 05327+3404. The lowest contour is  $0.525$   $\text{Jy beam}^{-1}$  with increments of  $0.35$   $\text{Jy beam}^{-1}$ . *b)* Map overlapping the higher relative velocity emission of the red- and blue-shifted channels, from  $-18.34$  to  $-15.80$   $\text{km s}^{-1}$  and from  $-26.72$  to  $-24.95$   $\text{km s}^{-1}$ , respectively. The first contour is at  $0.480$   $\text{Jy beam}^{-1}$ , with increments of  $0.32$   $\text{Jy beam}^{-1}$ . *c)* As panel *b)* overlapping the lower relative velocity emission of the red- and blue-shifted channels, from  $-20.63$  to  $-18.60$   $\text{km s}^{-1}$  and from  $-24.69$  to  $-22.66$   $\text{km s}^{-1}$ , respectively. The first contour is at  $0.750$   $\text{Jy beam}^{-1}$ , with increments of  $0.50$   $\text{Jy beam}^{-1}$ .

diagram also reveals two hyperbolic shapes at red- and blue-shifted channels, which could trace a possible keplerian rotation or infall. To explore this possibility, we tried to fit the centroid position of each velocity channel of the P-V plot with simulations of a keplerian rotating disk, within a range of central masses and inclinations. The best fits we found have  $M/\sin^2 i \sim 15 - 20M_{\odot}$ , and therefore seem to be incompatible with the mass determinations we have obtained from the dust continuum emission.

There could also exist the possibility that the NE outflow and part of the “E arm” of the E–W outflow are related forming a wide opening outflow. The coincidence of the directions of the NE outflow and the strong optical jet do not seem to support this, and neither does the good agreement in the morphology and physical parameters (see Table 2 and Sect. 4.2.1) between the red- and blue-shifted arms of the E–W outflow.

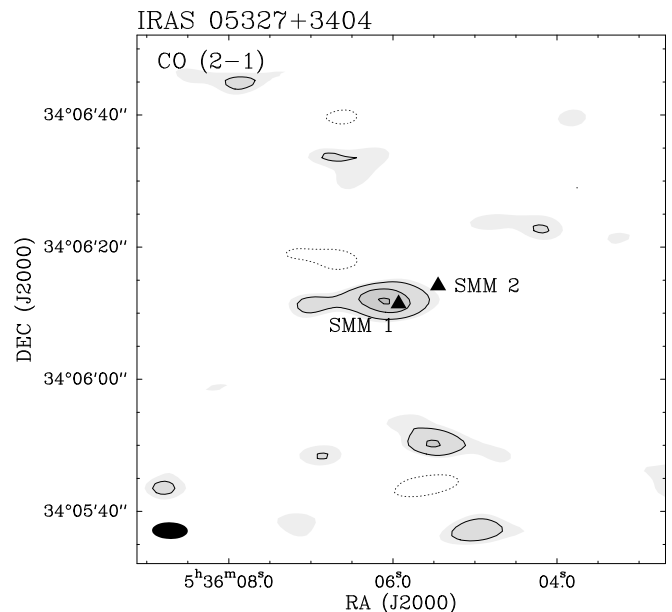


**Figure 11.** Integrated intensity map of the CO (2–1) emission in the velocity range from  $-25.0$  to  $-13.8$   $\text{km s}^{-1}$ , with a resulting mean velocity of  $-19.4$   $\text{km s}^{-1}$ . Contours are  $-3, 3, 6, 9, \dots$  times the rms of the map  $0.19$   $\text{Jy beam}^{-1}$ . The beam size is  $\sim 5''.4 \times 2''.5$ , with  $\text{PA}=88.8^{\circ}$ . The triangles mark the positions of the emission peaks in the 261 GHz continuum map (Fig. 1a).

Magnier et al. (1999b) suspected “Holoeca” to be an FU Orionis type star, which would explain the recorded increase in its luminosity in the last 40 years. FU Orionis stars are variable stars (Herbig 1977; Hartmann & Kenyon 1996), thought to be low-mass young stellar objects closer to Class I protostars than to Class II T Tauri stars (Sandell & Weintraub 2001; Herbig et al. 2003), that experience a brightening of up to 6 mag over a few months, followed by a much slower fading back to their original luminosity, linked to eruptions caused by the increase of several orders of magnitude in the mass accretion rate through the circumstellar disk around the star (Hartmann & Kenyon 1996; Hartmann et al. 2004; Reipurth & Aspin 2004). A few FU Oris, such as V1057 Cyg (Herbig et al. 2003; Reipurth & Aspin 2004) and V1331 Cyg (McMudroch et al. 1993; Quanz et al. 2007), show a shell of material around them, possibly as a consequence of an energetic mass ejection event (McMudroch et al. 1993). We do not find these structures in our observations or clear kinematic indications of shells expanding through the molecular gas surrounding IRAS 05327+3404.

#### 4.2.1. Mass and momentum of the CO outflows

Table 2 shows the estimated parameters of the two main outflows identified around IRAS 05327+3404: the East-West outflow around the position of SMM 1 and the NE outflow from the position of SMM 2. We present the parameters of the red- and blue-shifted arms of the East-West outflow, and the parameters of the red-shifted emission of the material that we identified as belonging to the NE outflow.

In order to calculate the mass of each outflow, we measured the flux inside the  $3\sigma$  contour of the integrated intensity maps where we could find emission belonging to

**Table 2**  
Physical parameters of the main CO (1–0) outflows found around IRAS 05327+3404

| Outflow  | $R_{\max}^a$<br>(pc) | $V_{\max}^b$<br>(km s <sup>-1</sup> ) | area <sup>c</sup><br>(arcsec <sup>2</sup> ) | $S_{\nu}$<br>(Jy) | $N_{\text{CO}}^d$<br>(cm <sup>-2</sup> ) | $M_{\text{out}}^e$<br>( $M_{\odot}$ ) | $t_d^f$<br>(10 <sup>4</sup> yr) | $\dot{M}_{\text{out}}^g$<br>( $M_{\odot}$ yr <sup>-1</sup> ) | $P_{\text{out}}^h$<br>( $M_{\odot}$ km s <sup>-1</sup> ) | $F_{\text{out}}^i$<br>( $M_{\odot}$ km s <sup>-1</sup> yr <sup>-1</sup> ) | $L_{\text{out}}^j$<br>( $L_{\odot}$ ) |
|----------|----------------------|---------------------------------------|---|-------------------|--|---------------------------------------|---------------------------------|--|--|---|---------------------------------------|
| E–W red  | 0.19                 | 5.8                                   | 416   | 9.90              | $1.6 \times 10^{16}$                     | 0.130                                 | 3.1                             | $4.2 \times 10^{-6}$   | 0.76   | $2.4 \times 10^{-5}$  | $2.3 \times 10^{-2}$                  |
| E–W blue | 0.15                 | 4.1                                   | 592   | 13.7              | $9.9 \times 10^{15}$                     | 0.117                                 | 3.6                             | $3.2 \times 10^{-6}$   | 0.48   | $1.3 \times 10^{-5}$  | $8.4 \times 10^{-3}$                  |
| NE red   | 0.24                 | 3.6                                   | 380   | 6.75              | $6.5 \times 10^{15}$                     | 0.049                                 | 6.7                             | $7.3 \times 10^{-7}$   | 0.17   | $2.6 \times 10^{-6}$  | $1.4 \times 10^{-3}$                  |

<sup>a</sup> Projected maximum size of the outflow at the  $3\sigma$  contour, adopting a distance  $D = 1.2$  kpc.

<sup>b</sup> Maximum relative velocity of the outflow, either red-shifted or blue-shifted, with respect to the systemic velocity.

<sup>c</sup> area in the sky inside the  $3\sigma$  contour of the integrated intensity maps over which the flux is measured.

<sup>d</sup> CO column density, calculated assuming local thermodynamical equilibrium (LTE) conditions.

<sup>e</sup> Mass traced by the outflow, calculated from  $M_{\text{out}}[M_{\odot}] = \bar{\mu} m_{\text{H}} \Omega_{\text{S}} D^2 N_{\text{CO}} / X[\text{CO}]$ , where  $\bar{\mu}$  is the average molecular weight, 2.33,  $m_{\text{H}}$  is the atomic hydrogen mass,  $\Omega_{\text{S}}$  is the solid angle of the source,  $D$  is the distance to the source, and  $X[\text{CO}]$  is the adopted CO abundance relative to  $\text{H}_2$ . We used  $X[\text{CO}] = 10^{-4}$  following Frerking et al. (1982).

<sup>f</sup> dynamical time scale of the outflow,  $t_d = R_{\max} / V_{\max}$

<sup>g</sup> mass outflow rate,  $\dot{M}_{\text{out}} = M_{\text{out}} / t_d$ .

<sup>h</sup> momentum of the outflow,  $P_{\text{out}} = M_{\text{out}} V_{\max}$ .

<sup>i</sup> momentum flux,  $F_{\text{out}} = P_{\text{out}} / t_d$ .

<sup>j</sup> outflow mechanical luminosity,  $L_{\text{out}} = 0.5 M_{\text{out}} V_{\max}^3 / R_{\max}$ .

each outflow: from  $-20.63$  to  $-15.81$  km s<sup>-1</sup> for the red-shifted arm of the E–W outflow, from  $-25.71$  to  $-22.66$  km s<sup>-1</sup> for the blue-shifted arm of the E–W outflow, and from  $-18.09$  to  $-20.63$  km s<sup>-1</sup> for the NE outflow. We estimated the CO column densities traced by the red- and blue-shifted channels adopting  $T_{\text{ex}} = 20$  K (Snell et al. 1984; Lada 1985; Aso et al. 2000), assuming local thermodynamical equilibrium conditions (LTE) and optically thin emission. Given the assumption of optically thin emission, the calculated column density values should be taken as a lower limit to the column density, because the lines are probably optically thick. For instance, Bontemps et al. (1996) adopted a mean factor of the opacity correction for the CO line of 3.5, following the detailed study of Cabrit & Bertout (1992). We have also chosen not to use any inclination angle,  $i$ , for the calculation of dynamical time scale, the mass outflow rate, the momentum of the outflow and the momentum flux. In the case of correcting for the inclination angle, the linear size should be divided by  $\sin i$ , and the velocities by  $\cos i$ . Magnier et al. (1996) estimated an inclination angle of  $i = 45^\circ$  for the NE outflow, but we do not have any additional information about the orientation of the E–W outflow with respect to the line of sight. Bontemps et al. (1996) estimate a mean correction factor of 2.9, corresponding to a random outflow orientation angle of  $57.3^\circ$  for the calculation of the CO momentum flux,  $F_{\text{out}}$ . Thus, following Bontemps et al. (1996) the corrected momentum flux of the outflows from Table 2, should be  $F_{\text{CO}} = 2.9 \times 3.5 \times F_{\text{out}} \sim 10 \times F_{\text{out}}$ , taking into account the corrections from opacity and the inclination angle mentioned above.

The resulting physical parameters (see Table 2) show that the E–W outflow appears to be more massive by a factor of 5, when adding the blue- and red-shifted arms, than the NE outflow. The dynamical time scale of the outflows is about a few times  $10^4$  yr, but the E–W outflow would have a shorter dynamical time scale by a factor of  $\sim 2$ . The rest of the physical parameters also show that the E–W outflow is a more powerful outflow than the NE outflow.

We compared the momentum flux derived for our outflows with the momentum flux vs. radio continuum luminosity correlation of Anglada (1996). We applied to  $F_{\text{out}}$  the correction factor of  $\sim 10$  used by Bontemps et al. (1996). Anglada & Rodríguez (2002) found a radio continuum luminosity of  $0.22$  mJy kpc<sup>2</sup> for their VLA 2 source. Unfortunately, the VLA observations were not able to resolve this source, but as we discussed in Sect. 3.1.1, it is safe to assume that all the centimeter emission comes from SMM 1 and that the contribution coming from SMM 2 is much smaller. In this case, we find that the radio continuum luminosity of VLA 2 (SMM 1) falls very well in the correlation with the calculated momentum flux of the E–W outflow. For SMM 2, we can assume a  $3\sigma$  upper limit for its associated radio centimeter continuum luminosity of  $< 0.1$  mJy kpc<sup>2</sup>. Following the correlation of Anglada (1996), the centimeter luminosity that we would obtain from the momentum flux of the NE outflow would be  $\sim 0.02$  mJy kpc<sup>2</sup>, and thus consistent with the VLA upper limit.

We also compared the physical parameters that we derived for our outflows with some of the results of Bontemps et al. (1996). First, we compared the corrected momentum flux of the outflows,  $F_{\text{out}}$ , vs the bolometric luminosity,  $L_{\text{bol}}$ . We find that the SMM 1 and the E–W outflow lie in the upper right corner of Fig. 5 of Bontemps et al. (1996), in the region associated with Class 0 sources, but relatively close to the best fit correlation found for Class I sources. The location of SMM 2 and the NE outflow is more uncertain, but it would be located in the Class I region, close to the best fit correlation for Class I objects if  $L_{\text{bol}} \sim 2\text{--}10 L_{\odot}$ . When we compared the momentum flux of the outflows with the mass of the circumstellar envelope derived in Sect. 4.1 with Fig. 6 of Bontemps et al. (1996), we found that SMM 1 is also located in the Class 0 YSOs region, and close to the best fit correlation for the Class I sources. On the other hand, SMM 2 and the NE outflow would be close to the region where there is the change from Class 0 to Class I sources.

Finally, we compared our data with the  $F_{\text{out}} c / L_{\text{bol}}$  vs  $M_{\text{env}} / L_{\text{bol}}^{0.6}$  plot shown in Fig. 7 of Bontemps et al.

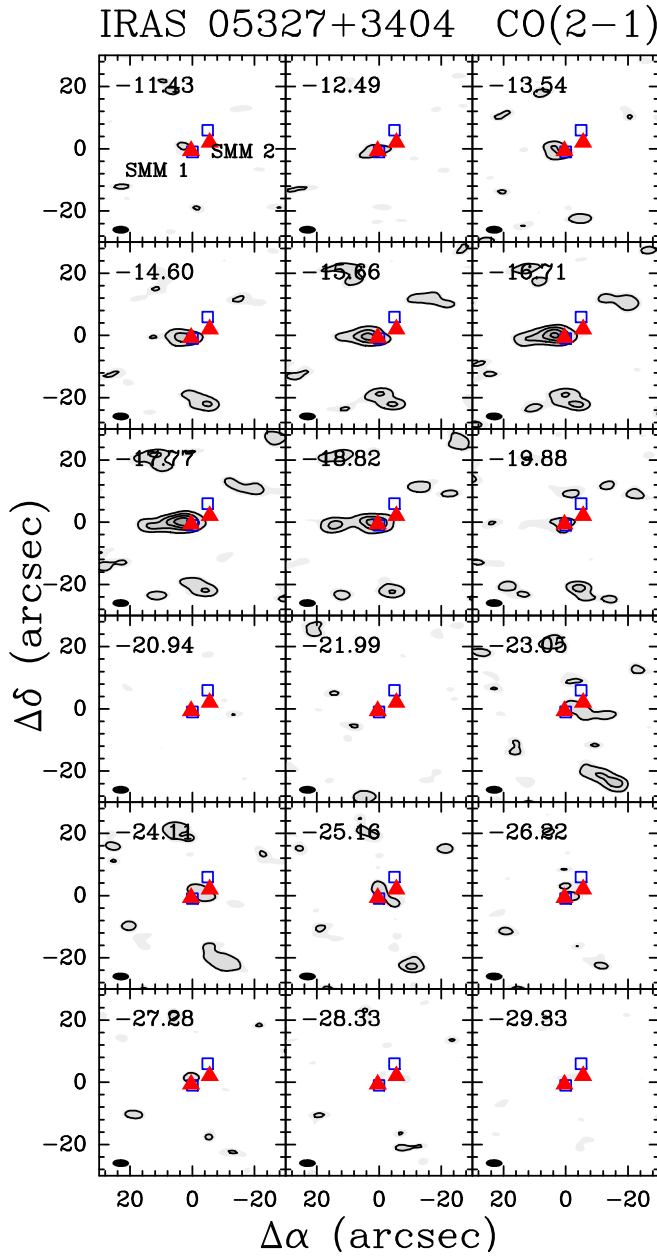


**Figure 12.** Maps of the 4-channel average of the CO (2–1) lines in the velocity interval from  $-29.83$  to  $-11.43$   $\text{km s}^{-1}$ . The contours are 3, 6, 9, ... times the rms of the map,  $0.25 \text{ Jy beam}^{-1}$ . The triangles mark the position of the continuum peaks and the squares mark the position of the  $\text{HCO}^+$  (3–2) emission peaks. The velocity, in  $\text{km s}^{-1}$ , of each map is indicated in the upper left corner of each panel.

(1996) that tries to remove luminosity effects from the momentum flux and the envelope mass. The efficiency of our outflows,  $F_{\text{out}}c/L_{\text{bol}}$ , is  $\sim 220\text{--}420$  for the E–W outflow, for SMM1 bolometric luminosities  $L_{\text{bol}}\sim 82\text{--}41 L_{\odot}$ , and between  $\sim 600\text{--}125$  for the NE outflow for luminosities of SMM 2  $\sim 2\text{--}10L_{\odot}$ . These values place SMM 1 in the region of the youngest Class I sources, and SMM 2 just at the transition between Class 0 and Class I YSOs. The location of SMM 2 is again much more uncertain due to our lack of knowledge about its bolometric luminosity.

We also compared the results we derived from the outflows around IRAS 05327+3404 with the sample of

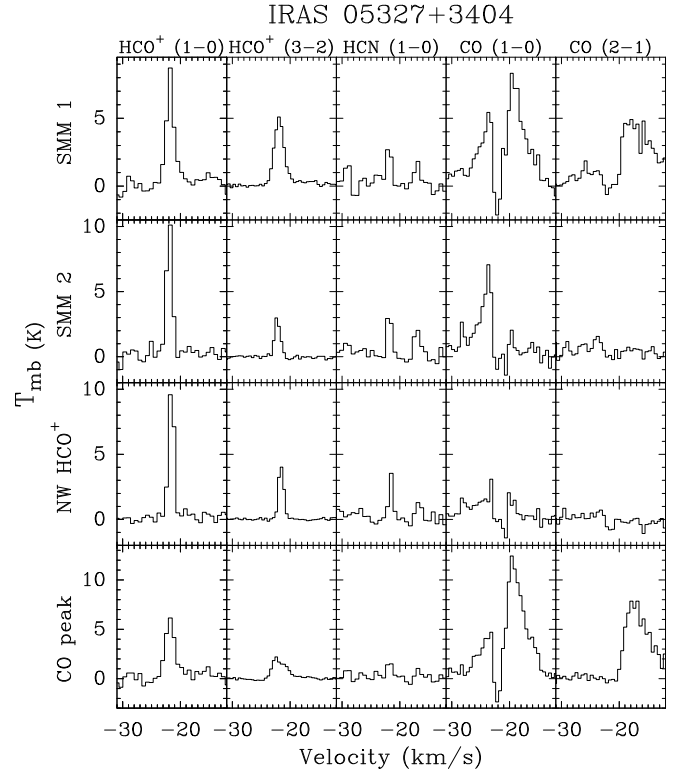


**Figure 13.** Spectra of the observed  $\text{HCO}^+$  (1–0),  $\text{HCO}^+$  (3–2),  $\text{HCN}$  (1–0),  $\text{CO}$  (1–0), and  $\text{CO}$  (2–1) lines obtained at four selected points of our maps.

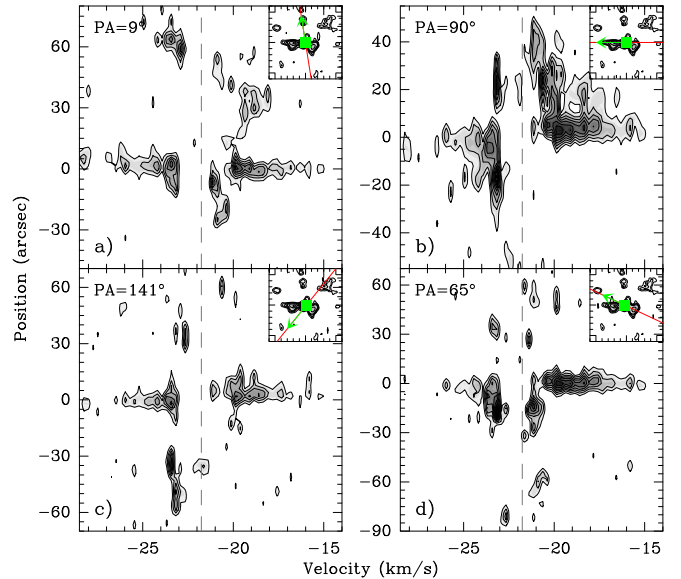


**Figure 14.** CO Position-Velocity cuts along four different position angles: *top left panel a)*  $\text{PA}=9^\circ$ , *top right panel b)*  $\text{PA}=90^\circ$ , *bottom left panel c)*  $\text{PA}=141^\circ$ , *bottom right panel d)*  $\text{PA}=65^\circ$ . The initial contour is at  $1.19 \text{ Jy beam}^{-1}$ , with increments of  $0.79 \text{ Jy beam}^{-1}$ . The dashed vertical line shows the position of the systemic velocity. The inset map for each figure shows the origin (green square) and direction of the P–V cut (green arrow over the red line) over the integrated intensity map of the corresponding transition. The position angle of the P–V cut is calculated with respect to the N direction. As a reference, positive positions correspond to the NE for  $\text{PA}=9^\circ$  and  $65^\circ$ , E for  $\text{PA}=90^\circ$ , and SE for  $\text{PA}=141^\circ$ .



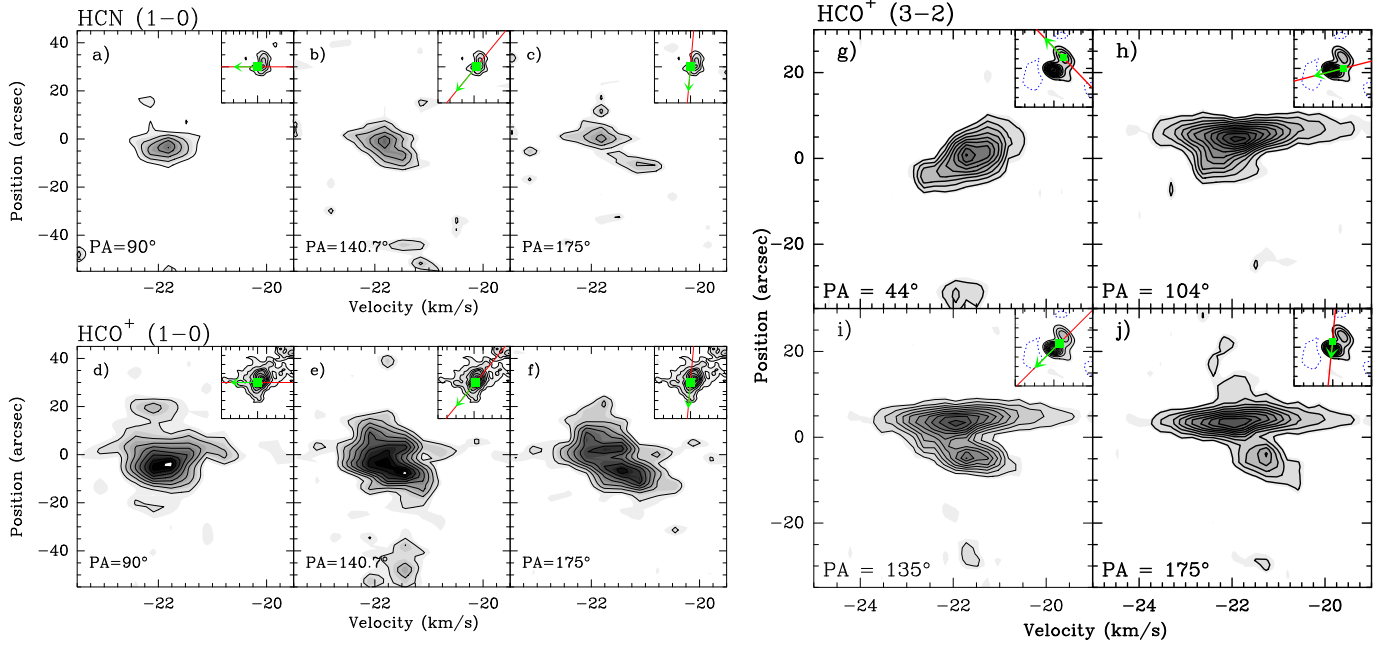


**Figure 15.** *Top left column)* Position-Velocity diagrams of the HCN (1–0) line along the directions: (a) PA= 90°, (b) PA= 140.7° and (c) PA= 175°. The initial contour is at 0.30 Jy beam<sup>-1</sup>, with increments of 0.20 Jy beam<sup>-1</sup>. *Bottom left column)* Position-Velocity diagrams of the HCO<sup>+</sup> (1–0) line along the directions: (d) PA= 90°, (e) PA= 140.7°, (f) PA= 175°. The initial contour is at 0.42 Jy beam<sup>-1</sup>, with increments of 0.28 Jy beam<sup>-1</sup>. *Right column)* Position-Velocity diagrams of the HCO<sup>+</sup> (3–2) line along the directions: (g) PA= 44°, (h) PA= 104°, (i) PA= 135°, and (j) PA= 175°. The initial contour is at 0.72 Jy beam<sup>-1</sup>, with increments of 0.72 Jy beam<sup>-1</sup>. The inset maps follow the same conventions as in Fig. 14.

Aso et al. (2000) of CO outflows in Orion. In a similar way, we find that the E–W outflow properties set the sub-mm source in the region occupied by what Aso et al. (2000) called “dark cloud Class 0” objects in the envelope mass vs momentum flux and bolometric luminosity vs. momentum flux plots. The location of SMM 2, more difficult to determine, would seem to be more in according with what Aso et al. (2000) called “dark cloud Class I” objects.

#### 4.3. Kinematic structures traced by HCO<sup>+</sup> and HCN

Figure 15 shows the Position-Velocity (P-V) cuts made for the HCN (1–0), HCO<sup>+</sup> (1–0), and HCO<sup>+</sup> (3–2) lines along some of the gas structures found in the integrated intensity maps. We find a velocity gradient in an approximately North–South direction, indicated by a velocity shift from  $\sim -22.4$  to  $-20.8$  km s<sup>-1</sup> for HCN and HCO<sup>+</sup> (1–0) in the P-V cuts following an almost N–S direction, PA= 175° (Fig. 15c and 15f). This velocity shift is also seen along the line connecting the two peaks in the integrated emission maps, PA= 140.7°, (Figs. 15b and 15e), but with a shallower gradient. The first order moment map of the HCO<sup>+</sup> (1–0) line (Fig. 16a) clearly shows this velocity gradient as a transition from red- to blue-shifted velocities in an approximately North–South direction. The P-V cuts done for the HCO<sup>+</sup> (3–2) line show similar results, but in this case, the extension is considerably reduced: Figs. 15i and 15j show the two condensations found in the integrated intensity maps and again the larger gradient is found for PA $\simeq$  175° (Fig. 15j). The first order moment map of the HCO<sup>+</sup> (3–2) emission (Fig. 16c) also shows the approximately North–South gradient found in HCO<sup>+</sup> (1–0) (Fig. 16a), but there is also a change in velocity East to South-West of SMM 1, that was not so clearly seen in the (1–0) line.

The P-V cut taken in a SW–NE direction along the major axis of the NW condensation for the HCO<sup>+</sup> (3–2) line (Fig. 15g), recovers the gradient shown in the HCO<sup>+</sup> (3–2) channel maps from  $\sim -22.5$  to  $\sim -21$  km s<sup>-1</sup> (Fig. 3). This P-V map shows a main condensation at a velocity  $\sim -21.7$  km s<sup>-1</sup>, corresponding to the HCO<sup>+</sup> (3–2) NW peak, and two emission plateaus that trace other structures. The first one is located  $\sim 5$  arcsec to the NE at  $\sim -21.1$  km s<sup>-1</sup> and it is also found in the P-V cut with PA= 175° (Fig. 15j). The second one is located  $\sim 4$  arcsec to the SW, at  $\sim -22.3$  km s<sup>-1</sup>, is also found in the P-V cut connecting SMM 1 and SMM 2 (PA $\simeq$  104°), and would correspond to SMM 2. (Fig. 15h).

The HCO<sup>+</sup> (3–2) P-V cuts show much more clearly a line broadening of  $\sim 2$  km s<sup>-1</sup> at a position of  $\sim 2$ – $3$  arcsec East of the main HCO<sup>+</sup> emission peak. This is close to the position of the main CO (1–0) peak and the broadening could indicate the presence of some shocks at this position, but it could also be related to rotation or even collapse. This effect is outstanding in the second order maps of the HCO<sup>+</sup> lines (Fig. 16b and 16d). HCO<sup>+</sup> line-widths are  $\sim 0.4$ – $0.6$  km s<sup>-1</sup> for most of the map except for a region 6 arcsec in size East of SMM 1. The HCO<sup>+</sup> (3–2) spectra on this part of the map show a complex structure, with shoulders on the line wings and maybe more than one component. Line-widths can be as wide as 2.9 km s<sup>-1</sup>. If the line-widths corresponded to a rotational flow, we estimate, following Lada (1985), that we would need a mass  $M > 8M_{\odot}$  interior to the flow to support it, or  $\sim 25M_{\odot}$  to have a bound self-gravitating structure, which is several times larger than the mass traced by the dust continuum. Therefore, the gas traced by HCO<sup>+</sup> close to SMM 1 is probably gas affected by the local outflows. We do not find any HCO<sup>+</sup> line broadening

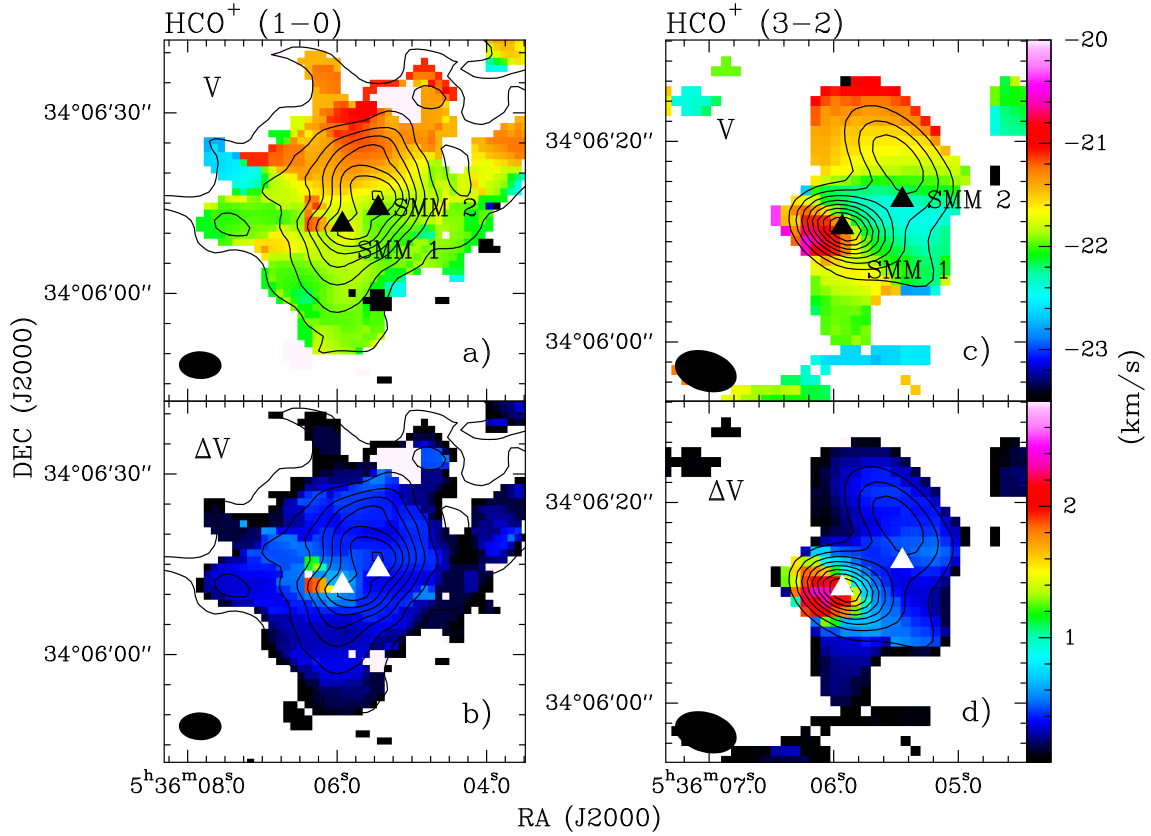


**Figure 16.** Maps of the first (*top row*) and second order (*bottom row*) moments of the  $\text{HCO}^+$  (1–0) (*left column*) and (3–2) (*right column*) emission overlaid with the corresponding integrated intensity map in IRAS 05327+3404. The triangles mark the position of the continuum sources SMM 1 and SMM 2.

in the parts of the map to the North where there is redshifted  $\text{HCO}^+$  emission.

Finally, the P-V cuts along a direction with  $\text{PA} \simeq 175^\circ$  of the  $\text{HCO}^+$  and HCN lines (Figs. 15c, 15f and 15j) also find traces of weak emission  $\sim 10$  arcsec South of SMM 1, which would correspond to the very weak condensation found in the respective channel maps. We also find weak emission  $\sim 20$  arcsec East of the central position of the map in the P-V cuts made in a direction East–West,  $\text{PA} = 90^\circ$ , through the position of the  $\text{HCO}^+$  peak (Figs. 15d and 15a). This would correspond to the weak emission found in  $\text{HCO}^+$  (1–0) coinciding with a local peak of CO (1–0). It is unclear what is the nature of these objects, probably gas in some stage of pre-stellar core or other clumpiness of the cloud.

#### 4.4. The distribution of the molecular gas

Figure 17 shows the superposition of the integrated intensity maps of the CO,  $\text{HCO}^+$ , and HCN emissions obtained from the BIMA observation, mainly showing the gas distribution at larger scales. Figure 18 shows a similar map zoomed in at smaller scales in order to compare the BIMA and SMA observations.

The bulk of the more intense HCN and  $\text{HCO}^+$  emission, which will trace the denser component of the molecular gas, is found in a central region,  $\sim 20 \times 15$  arcsec in size and it encompasses the sub-mm continuum emission and the two SMM sources, SMM 1 and 2. Lower density gas probably surrounds this central region, as it is traced by the weak  $\text{HCO}^+$  (1–0) component. The CO lines seem to trace mostly the molecular outflows.

The molecular emission peaks show a large degree of coincidence amongst themselves and with the positions of the SMM sources: two of the  $\text{HCO}^+$  peaks coincide with the SMM sources, while the third one (the one we named NW  $\text{HCO}^+$ ) also coincide with the northern HCN plateau. Only the HCN emission peak seems to be located in-between SMM 1 and SMM 2. Thus, the molecular and continuum data show that there are multiple objects in the region. Two of these objects are probably proto-stars, because of the detected sub-millimeter emission and its alignment with some of the high-velocity structures found in CO. The third condensation, only found in the  $\text{HCO}^+$  and HCN lines, is either a starless or pre-stellar core; too cold to show a sub-millimeter peak.

There are other minor emission peaks in our maps: a local CO (1–0) emission peak that coincides with a  $6\sigma$  peak of the  $\text{HCO}^+$  (1–0) line at  $\sim 18$  arcsec East of IRAS 05327+3404, and the hint of another possible condensation seen in the channel maps of  $\text{HCO}^+$  (1–0) and (3–2) located  $\sim 10$  arcsec S of SMM 1.

##### 4.4.1. The missing CO emission

There are probably different reasons to explain the big difference between CO and the other molecules, and why it is concentrated in a relatively East-West strip. CO traces lower density material than  $\text{HCO}^+$  and HCN, and thus CO emission should be more widespread over the region. This makes it more likely to suffer from missing flux effects. From the low intensity distribution of the  $\text{HCO}^+$  (1–0) emission, we would expect that CO would be distributed all around the molecular core, but most of

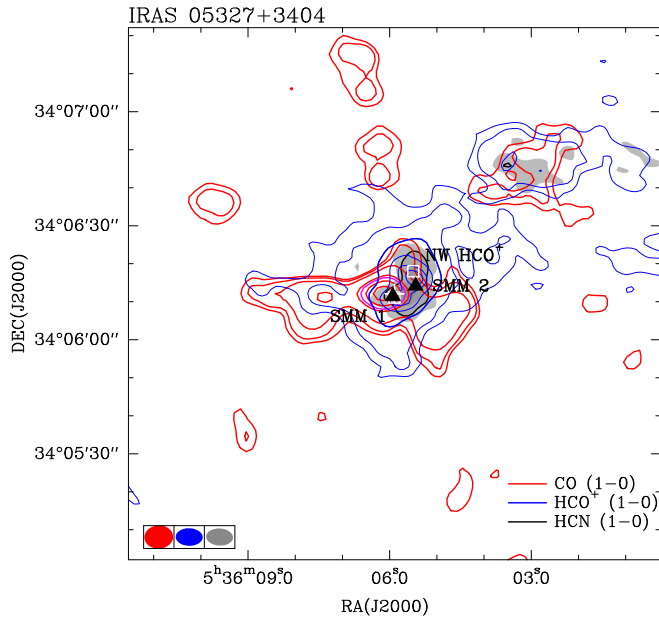


**Figure 17.** Integrated intensity emission of the CO (1–0) (red contours),  $\text{HCO}^+$  (1–0) (blue contours), and HCN (1–0) (gray scale and one black contour at FWHM) emission, in the velocity intervals  $-27.47$  to  $-15.04$   $\text{km s}^{-1}$ ,  $-22.42$  to  $-20.78$   $\text{km s}^{-1}$ , and  $-22.15$  to  $-21.15$   $\text{km s}^{-1}$ , respectively. The triangles mark the position of the continuum peaks and the squares the position of the  $\text{HCO}^+$  (3–2) peaks.

the emission is probably filtered out by the interferometer. The integrated intensity map of CO mainly traces high-velocity gas (Fig. 9), which we expect would suffer less from filtering-out by the interferometer as it would be relatively more compact, and most of the CO emission we observe is probably due to molecular outflow emission. As a consequence (see Sect. 3.2.4), we do not find CO (1–0) emission around the systemic velocities almost anywhere in our map. This prevents any chance of disentangling the relationship between the high-velocity and “quiescent” CO gas in the region.

We took several spectra along the East–West direction on both sides of the CO integrated intensity maximum (Fig. 19), in order to study the missing CO emission. The line emission in the spectra moves from mostly blue-shifted to the West of the emission peak (spectra “a” and “b”) to mostly red-shifted to the East (spectra “f” and “g”), with a gradual decrease of blue-shifted emission and an increase of red-shifted emission from the “c” to the “e” spectra. All these spectra show missing CO emission around the systemic velocities ( $-21.7$   $\text{km s}^{-1}$ ), where we find what seems to be a more or less deep absorption feature in most of them. Only the farthest positions, “a” and “i”, might not show this absorption feature.

The spectral data could be indicating that there is an extended foreground, and colder, gas component surrounding the core revealed by  $\text{HCO}^+$  and HCN, which is responsible for absorbing the CO emission. However, this absorption feature should also be apparent in single-dish observations, but that is not the case for the spectra of the CO (2–1) line of Magnier et al. (1996). Thus, we conclude that the interferometers mostly detect the CO components related to the outflows (relatively more compact and less subject to filtering out).

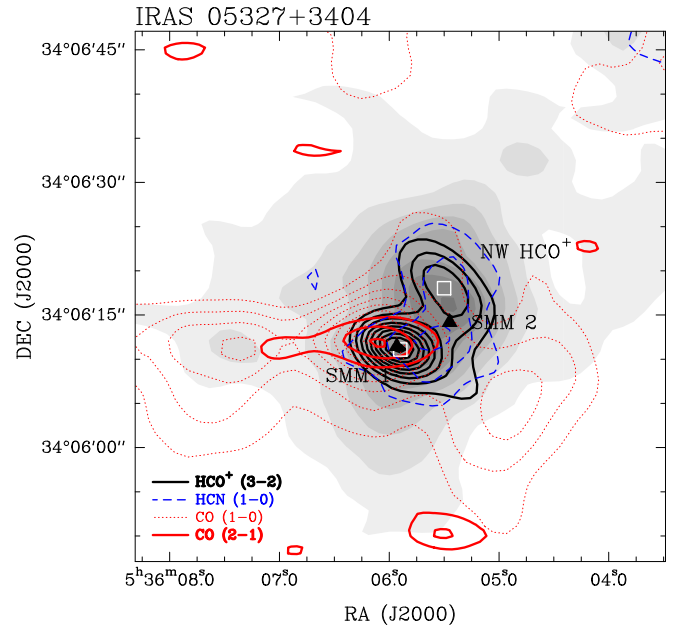


**Figure 18.** Integrated intensity emission of the  $\text{HCO}^+$  (3–2) line (thick black contours) overlaid over the integrated intensity of the CO (2–1) line (thick red contours), the integrated intensity map of  $\text{HCO}^+$  (1–0) (gray scale), the integrated intensity map of HCN (1–0) (dashed blue contours) and the integrated intensity map of CO (1–0) (dotted red contours). The triangles mark the position of the continuum peaks SMM 1 and SMM 2, and the squares, the position of the  $\text{HCO}^+$  (3–2) peaks.

#### 4.5. The structure of the region and the nature of the powering sources

The millimetric and sub-millimetric observations show that the properties and the structure of the gas around the position of IRAS 05327+3404 “Holoëa” are much more complicated than previously thought.

The data are helpful in the description of the morphology and the identification of existing proto-stellar objects, allow us to characterize several molecular outflows and argue for an identification of the respective powering sources. Nonetheless, our data cannot give any conclusive determination for several other velocity structures found in the region, and the possibility that there exist more embedded sources is still open.

Magnier et al. (1996) discussed three possible toy models that could describe the physical structure of M36 “Holoëa”. They favored an scenario in-between two of those models, in which there would be a molecular outflow powered by the star, with the red-shifted gas not moving in a well-collimated jet, but it would be spraying in a wide range of directions, or the presence of a thick disk around the star, IRAS 05327+3404, would shadow the south-pointing jet and outflow and we would only see the south-side emission far from the star and at lower velocities. They also discussed the possibility that the system could be a binary (Magnier et al. 1999b) in order to explain some of the properties of the observed SED.

From the results of our data, we favor a different interpretation of the structure of the region. Our continuum data show that there are two sub-millimetric sources in the region, SMM 1 and SMM 2, separated by  $\sim 6$  arcsec ( $\sim 7300$  AU), which would be powering the two main outflows we identify in the CO (1–0) observations: SMM 1 would be powering the East-West bipolar out-



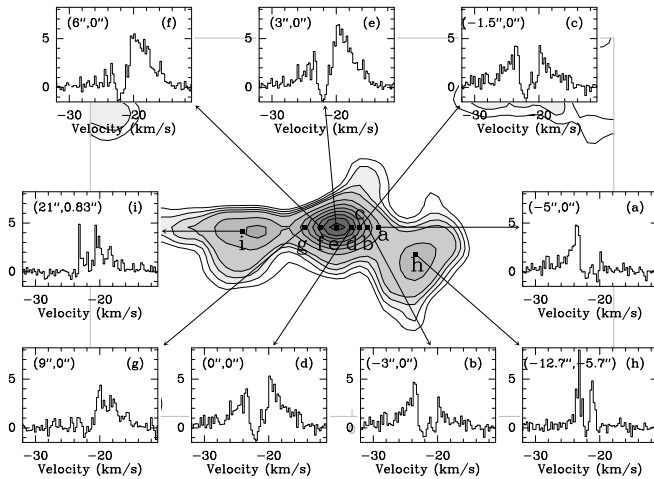


**Figure 19.** CO spectra, in units of  $\text{Jy beam}^{-1}$ , taken at nine different positions on both sides of the CO (1-0) emission peak of IRAS 05327+3404. The offset positions are referenced to the nominal position of IRAS 05327+3404.

flow, while SMM 2 would be the powering source of the NE red-shifted outflow. The orientation of both outflows would be different with respect to the line of sight, undetermined for the E–W outflow, while the NE outflow could have an inclination angle,  $i = 45^\circ$  (Magnier et al. 1999b). The blue-shifted counterpart of the NE outflow is not visible, maybe because its emission is confused with the blue-shifted lobe of the E–W outflow. Our data is not good enough to distinguish that, although this last possibility seems to be unlikely.

The gas surrounding the two SMM objects would have masses from a few tenths of solar masses ( $\sim 0.8 M_\odot$  for SMM 2) up to  $1\text{--}2 M_\odot$  ( $\sim 1.5 M_\odot$  for SMM 1). Additionally, the  $\text{HCO}^+$  (1-0),  $\text{HCO}^+$  (3-2), and  $\text{HCN}$  (1-0) lines also have emission peaks approximately coinciding with these two objects, which confirms that the SMM sources are associated with dense gas. The comparison we have been able to do between the  $L_{\text{bol}}$  measured by Magnier et al. (1996), the envelope masses and the outflow parameters we derived for our objects, allows us to guess an evolutionary stage for both SMM sources. SMM 1 would be in a Class 0, probably very early Class I, stage as indicated by the outflow parameters and the relationship between the bolometric luminosity and the envelope mass. SMM 2 seems to be in a more advanced stage of evolution, advanced Class I probably, given the weaker molecular outflow and its outflow parameters. Additionally, SMM 1 seems to be related to a denser gas, traced by the continuum and high-density tracers, while SMM 2 seems to be in a slightly less dense environment. This also supports the earlier evolutionary stage for SMM 1. Thus, we think that our data rather shows that the *two SMM sources are in an earlier evolutionary stage than previously expected, probably early Class I stage*. We must be cautious though, given the uncertainties related to the calculation of the outflow parameters, the difficulties in the determination of the bolometric luminosity of each object, and the general complex kinematic structure of the region.

There would be another object located close to the two SMM sources,  $\sim 8.5$  arcsec NW of SMM 2 (see Sect. 3.2.1), as detected by the  $\text{HCO}^+$  and  $\text{HCN}$  lines. This object is not detected in the continuum, which sug-

gests that it is probably a pre-stellar core or some cold embedded object. Interestingly, this core is also aligned with the direction of the NE outflow, but the lack of continuum emission associated with this object would a priori preclude it to be considered a candidate to be the powering source of any outflow. Additionally, there are two other condensations visible in some of the  $\text{HCO}^+$ ,  $\text{HCN}$ , and  $\text{CO}$  data, but not associated with continuum emission: one is located  $\sim 18$  arcsec East of SMM 1 and the other  $\sim 10$  arcsec South of SMM 1. With the limited amount of information that we have, these two condensations seem to be just two candidate starless cores.

Magnier et al. (1999b) proposed that the system they found could be a binary, which is a possibility given the short projected distance between the SMM sources. Additionally, we also found a velocity gradient in the North–South direction, at a scale of  $\sim 40$  arcsec, and another gradient in the gas around the NW  $\text{HCO}^+$  position. These gradients suggest some internal motions, but there does not seem to be any significant relative motion between SMM 1 and SMM 2.

## 5. CONCLUSIONS

We observed the object named “Holoera”, associated with the IRAS 05327+3404 source in M36, with the SMA telescope at 1.1-mm, using the CO (2-1) and  $\text{HCO}^+$  (3-2) lines, and with the BIMA telescope at 3-mm using the CO (1-0),  $\text{HCO}^+$  (1-0), and  $\text{HCN}$  (1-0) lines. This object had been identified by Magnier et al. (1996, 1999b) as a candidate transitional YSO between Class I and Class II with several unusual properties. We detected the emission of the three molecules, but they show a markedly different distribution. We also detected dust continuum emission at 1.1-mm in the SMA observations.

The continuum emission reveals two sub-millimeter peaks: the more intense one, SMM 1, with a flux density of  $39.1 \text{ Jy}$ , coincides within uncertainties with the nominal position of IRAS 05327+3404 and with the VLA 2 source of Anglada & Rodríguez (2002), and we identify it as the sub-mm counterpart of the IRAS source. The second sub-mm emission peak, SMM 2, with a flux density of  $19.9 \text{ Jy}$ , is located  $\sim 6$  arcsec to the NW of SMM 1. From the dust emission, we calculated a mass of  $1.5 M_\odot$  for SMM 1 and  $0.8 M_\odot$  for SMM 2.

The distribution of the  $\text{HCO}^+$  (1-0), (3-2), and  $\text{HCN}$  (1-0) emissions is more centrally concentrated, as it is expected for these molecular tracers, and they show at least two emission peaks. The main emission peak of the  $\text{HCO}^+$  lines is found around the position of SMM 1, another  $\text{HCO}^+$  (3-2) emission peak coincides with SMM 2, and there is a third peak, located  $8.5$  arcsec to the NW of SMM 1, not found in the continuum data, which is also present in the  $\text{HCO}^+$  and  $\text{HCN}$  data. Thus, there is evidence of at least two proto-stellar objects and a third possible pre-stellar condensation. The integrated CO (1-0) emission is mainly found in an E–W direction, with the intensity peak  $\sim 3$  arcsec East of the position of SMM 1. The CO lines around the central position show a dip in the intensity, which we attribute to the filtering out of extended emission by the interferometers.

We found several different velocity components in the red- and blue-shifted channels of the molecular lines. We identify two main molecular outflows in the region: a bipolar CO outflow elongated in an East–West direction



with the blue- and red-shifted lobes overlapping over the position of SMM 1, which was also detected at lower angular resolution by Magnier et al. (1999b); and an outflow in the NE direction (PA= 9°), only found at red-shifted velocities, pointing to the position of SMM 2, in approximately the same direction as the outflow detected by Magnier et al. (1999b). We identify SMM 1 as the best candidate to be the powering source of the E–W outflow, while SMM 2 could be the powering source of the NE outflow and the embedded YSO proposed by Magnier et al. (1999b). We find other high-velocity structures around the central part of the map, and evidence of line broadening due to shocks and/or outflows in the CO and HCO<sup>+</sup> spectra, that might point to the presence of a third outflow or simply to the interaction of the E–W outflow with the surrounding gas. The sensitivity and angular resolution of our data does not allow us to avoid the confusion in the region.

From the determination of the physical parameters of the two molecular outflows and the SMM objects, we have also been able to look into the evolutionary stage of the YSOs. We propose that SMM 1 is in an earlier evolutionary stage than SMM 2, and probably in an early Class I phase. SMM 2 seems to be in a more advanced stage of the Class I phase, but probably not by much.

The general picture that we propose for the region is that it is a more complex system than it was thought, with at least two YSOs, which are powering the two main outflows detected in our CO channel maps. There could be more objects in the region, and additional outflows, but the detailed structure is very difficult to disentangle with the data available to us. Most of these objects are probably embedded, except “Holoa”, which is beginning to be revealed, probably by the progressive clearing of the gas by one (or several) of the detected molecular outflows. Further multi-wavelength (optical, NIR, sub-millimetric) observations are needed to obtain a more precise description of the structure of the objects and of the physical processes that are taking part in them.

We thank Alfonso Trejo for the help provided to retrieve the SMA filler-time data, and Glen Petitpas and Chunhua Qi for help in the reduction of the SMA data. We thank Ming-Fan Ho for his work on the BIMA data. O. M. is supported by the NSC (Taiwan) ALMA-T grant to the Institute of Astronomy & Astrophysics, Academia Sinica. The research of Y.-J. K. was supported by NSC

99-2112-M-003-003-MY3 grant.

*Facilities:* BIMA, SMA

## REFERENCES

- Adams, F. C., Lada, C. J., & Shu, F. H. 1987, *ApJ*, 312, 788  
 André, P., Ward-Thompson, D., & M., B. 1993, *ApJ*, 406, 122  
 Anglada, G. 1996, in *Astronomical Society of the Pacific Conference Series*, Vol. 93, *Radio Emission from the Stars and the Sun*, ed. A. R. Taylor & J. M. Paredes, 3–14  
 Anglada, G., & Rodríguez, L. F. 2002, *RMxAA*, 38, 13  
 Aso, Y., Tatematsu, K., Sekimoto, Y., Nakano, T., Umemoto, T., Koyama, K., & Yamamoto, S. 2000, *ApJS*, 131, 465  
 Blitz, L., Fich, M., & Stark, A. A. 1982, *ApJS*, 49, 183  
 Bontemps, S., Andre, P., Terebey, S., & Cabrit, S. 1996, *A&A*, 311, 858  
 Cabrit, S., & Bertout, C. 1992, *A&A*, 261, 274  
 Codella, C., Palumbo, G. G. C., Pareschi, G., Scappini, F., Caselli, P., & Attolini, M. R. 1995, *MNRAS*, 276, 57  
 Frau, P., et al. 2010, *ApJ*, 723, 1665  
 Frerking, M., Langer, W. D., & Wilson, R. W. 1982, *ApJ*, 262, 590  
 Hartmann, L., Hinkle, K., & Calvet, N. 2004, *ApJ*, 609, 906  
 Hartmann, L., & Kenyon, S. J. 1996, *ARA&A*, 34, 207  
 Herbig, G. H. 1977, *ApJ*, 217, 693  
 Herbig, G. H., Petrov, P. P., & Duemmler, R. 2003, *ApJ*, 595, 384  
 Ho, P. T. P., Moran, J. M., & Lo, K. Y. 2004, *ApJ*, 616, L1  
 Hron, J. 1987, *A&A*, 176, 34  
 Lada, C. J. 1985, *ARA&A*, 23, 267  
 Lada, C. J., & Wilking, B. A. 1984, *ApJ*, 287, 610  
 Magnier, E. A., Volp, A. W., Laan, M. E., van den Ancker, M. E., & Waters, L. B. F. M. 1999a, *A&A*, 352, 228  
 Magnier, E. A., Waters, L. B. F. M., Groot, P. J., van den Ancker, M. E., Kuan, Y.-J., & Martín, E. L. 1999b, *A&A*, 346, 441  
 Magnier, E. A., Waters, L. B. F. M., Kuan, Y.-J., Chu, Y.-H., Taylor, A. R., Matthews, H. E., & Martín, E. L. 1996, *A&A*, 305, 936  
 McMuldroch, S., Sargent, A. I., & Blake, G. A. 1993, *AJ*, 106, 2477  
 Ossenkopf, V., & Henning, T. 1994, *A&A*, 291, 943  
 Quanz, S. P., D., A., & Henning, T. 2007, *ApJ*, 656, 287  
 Reipurth, B., & Aspin, C. 2004, *ApJ*, 608, L65  
 Sandell, G., & Weintraub, D. A. 2001, *ApJSS*, 134, 115  
 Sault, R. J., Teuben, P. J., & Wright, M. C. H. 1995, in *Astronomical Data Analysis Software and Systems IV*, ed. R. A. Shaw, H. E. Payne, and J. J. Hayes (San Francisco: Astronomical Society of the Pacific), *ASP Conf. Ser.*, 77, 433  
 Snell, R. L., Scoville, N. Z., Sanders, D. B., & Erickson, N. R. 1984, *ApJ*, 284, 176  
 Sunada, K., Nakazato, T., Ikeda, N., Hongo, S., Kitamura, Y., & Yang, J. 2007, *PASJ*, 59, 1185  
 Ward-Thompson, D. 1996, *Ap&SS*, 239, 151  
 Wouterloot, J. G. A., Brand, J., & Fiegle, K. 1993, *A&ASS*, 98, 589